Surface and Interface Physics Driven by Quantum Materials

Shuji Hasegawa[1]*

[1]*Department of Physics, University of Tokyo, Tokyo 113-0033, Japan*

*E-mail: shuji@phys.s.u-tokyo.ac.jp

Electronic states at boundaries of crystals, such as surfaces, interfaces, edges, hinges, corners, and extremities, play crucial roles in emerging quantum materials like graphene and similar monatomic-layer materials, van der Waals crystals, and topological insulators. Electronic states at such boundaries are different from those inside the three- or two-dimensional crystals, not only due to the truncation of crystal lattices, but also due to space-inversion-symmetry breaking and difference of topology in band structures across the boundaries. Such quantum materials are expected to advance energy-saving/-harvesting technology as well as quantum computing/information technology because of exotic phenomena such as electron's spin-momentum locking, pure spin current, dissipation-less charge current, non-reciprocal current, possible Majorana fermions, and so on. In this review, their fundamental concepts are introduced from the viewpoint of surface physics, in which atomic and electronic structures as well as charge/spin transport properties are directly probed using state-of-art techniques.

1. Introduction

Long before the research boom about topological insulators, it has been well known that there exist, in general, electronic states at crystal surfaces, "surface states", that have properties different from those inside three-dimensional (3D) crystals. For example, Si(111) surface with 7×7 reconstruction has a metallic surface state within the Si bulk band gap [1], which is due to unpaired electrons at dangling bonds of the topmost Si atoms on the surface. This kind of surface states, which are traditionally called by "Tamm states" and "Shockley states" [2-4], originate from truncation of crystal-lattice periodicity and asymmetric electrostatic potentials at the crystal surfaces.

Topology in band structures of 3D crystals, on one hand, are now a target of intensive research in condensed matter physics [5,6]; some of insulators/semiconductors have "negative band gaps" in the band structure due to "band inversion" in which the bottom of conduction band and the top of valence band are exchanged in energy position, resulting in the parity mixing in the wavefunctions of conduction/valence band electrons (called a "non-trivial" band structure). Since vacuum is one of trivial insulators (with an energy gap for electron-positron pair creation), the surface of a topological insulator crystals is a boundary between the non-trivial insulators and the trivial insulator (vacuum), resulting in a metallic surface state connecting the valence and conduction bands across the bulk band gap of the topological insulators. Therefore, the origin of the surface states on topological insulators, "topological surface states", is totally different from the traditional Tamm/Shockley surface states.

The topological surface states never disappear by contamination/oxidation/degradation of the crystal surfaces unless the non-trivial band structures inside the crystals change into trivial. When the surface layer of a topological insulator crystal is, for example, oxidized to form a trivial oxide layer, the topological surface states survive by shifting them from the top surface to an interface between the oxide layer and bulk topological insulator. This robustness is totally different from the characters of traditional Tamm/Shockley states which disappear easily by surface oxidation/contamination; the metallic dangling-bond states of the Si(111)-7 × 7 surface easily disappear by oxidation or adsorption of other atoms. An interface between a topological insulator and a trivial material always has the metallic topological states localized at the interface. Be noticed that, though the topological surface states are robust, the transport through the states is degraded by defects and impurities there.

The band inversion occurs inside the topological insulator crystals due to strong spin-orbit interaction (SOI), resulting in the metallic topological surface states having spin-helical "Dirac cones". The Dirac cone is a linear band dispersion described by relativistic Dirac equation with zero mass, which is famous for graphene [7-10] and is in strong contrast to usual free electrons having a parabolic band dispersion described by Schrödinger equation. While, however, the Dirac cone at graphene is spin-degenerate because of negligible SOI, the spin-helical Dirac cones of topological insulators' surface states have a unique character of "spin-momentum locking" in which the spin of an electron is always polarized in a

direction perpendicular to the momentum of the electron. This means that electrons flowing in opposite directions have opposite spins, resulting in "pure spin current", a flow of spin angular momentum, while charge current is canceled out due to opposite flows of electrons. In other words, pure spin current always flows on the surface of topological insulator crystals because electrons move around on the crystal surface, resulting in canceling out with each other to produce no net charge current, leaving pure spin current. Furthermore, 180°-back elastic scattering of the surface-state electrons never occurs unless the spin is flipped at the scattering. The momentum and spin are so strongly locked with each other that the scattering of surface carriers in different directions must accompany the change of spin direction. This is in strong contrast to ordinary materials with negligible SOI in which carrier scattering occurs without restriction by spin.

Two-dimensional (2D) topological insulators [11-14] have metallic edge states by the same reason as in 3D topological insulators; in the helical edge states, pure spin current flows without energy dissipation. "Topological superconductors" [15,16], which is beyond the framework of Bardeen-Cooper-Schriefer (BCS) theory, have edge states hosting an exotic "Majorana fermions" in the superconducting gap.

Because of these unique properties, topological insulators as well as graphene are intensively studied around the world not only for fundamental research of condensed matter physics, but also for possible applications to devices aiming novel technology. Especially their surfaces and interfaces are main playgrounds for charge/spin transport physics. In this review, fundamental concepts of their physics are introduced from the viewpoint of surface physics, together with some typical examples.

2. Surface electronic states

As shown in Fig. 1, there are various kinds of reasons why the electronic states at crystal surfaces are different from those inside 3D bulk crystals. In metals (a), electrons behave as Bloch wave in the crystal, a part of which spills out into vacuum from the crystal surface, so that the electronic energy levels at the surface can be different from those inside the crystal. In semiconductors in which covalent bonds make the crystal lattice (b), there exist unpaired electrons, called "dangling bonds", at the crystal surface, so that the electronic states at the surface are again different from those inside the crystal. By adsorbing foreign atoms on the

crystal surface (c), kinds of "surface alloys" can be formed by mixing the atoms of substrate and adsorbates together, resulting in unique electronic states there. The substrate sometimes acts as a catalysis to form a two-dimensional (2D) atomic sheet made of the adsorbate atoms, such as graphene [17] and graphene-like atomic-layer materials, Silicene [18], Germanene [19], Stanene [20], Plumbene [21], and so on; they have their own atomic structures and electronic states which are totally different from those of the substrates and their 3D counterparts. On the surface of topological insulators (d), as mentioned in the previous section, there exist metallic surface states because of an inevitable interface between topologically non-trivial-band region inside the crystal and trivial-band region outside (vacuum); the origin is totally different from those of other types of surface states.

The surface states, most of which are located inside energy gaps of the 3D bulk bands of substrates, have various kinds of dispersion and spin-degenerate/spin-split properties, as schematically shown in Fig. 2. For example, monatomic Ag layer on Si(111) showing Si(111)-$\sqrt{3} \times \sqrt{3}$-Ag surface superstructure (a) has a parabolic surface-state band with spin-degenerate in the band gap of Si substrate [22]. A monatomic layer of graphene grown in SiC(0001) crystal surface (b), shows linear dispersion with spin-degenerate, so called "Dirac cone" inside the band gap of SiC substrate [23]. The surface of a heavy metal crystal such as Au(111) (c), has spin-split parabolic bands by so-called Rashba effect due to strong SOI [24]. A monolayer alloy of Tl and Pb atoms formed on Si(111) surface is also an example of Rashba-type spin splitting [25,26]. The surface state of a topological insulator such as Bi_2Se_3(111) is a spin-helical Dirac cone (d), in which the opposite branch in the Dirac cone has opposite spin due to spin-momentum locking [27,28]. 2D topological insulators have helical one-dimensional (1D) edge states having similar linear dispersions in which opposite flows of electrons having opposite spins, leaving pure spin current [13]. A magnetic topological insulator such as $MnBi_2Se_4$ (e), has a surface state of a "gapped" spin-helical Dirac cone [29,30], resulting in a 1D chiral edge state inside the gap, which is located at the periphery of surface where dissipation-less charge current flows in one direction along the edge of the surface, called quantum anomalous Hall effect [31]. Therefore, the surface states, or boundary states in more general, are interesting platforms for condensed matter physics and possible device applications. All of them are shown in the following sections with some examples.

3. Spin-degenerate surface states

Schrödinger-electrons states

A monatomic layer of Ag atoms adsorbed on Si(111) surface, showing Si(111)-$\sqrt{3} \times \sqrt{3}$-Ag surface superstructure (Fig. 3) [22], has been well studied about its atomic arrangement (a), electronic band structure (b)-(d), and electrical transport property (f). The topmost Si atoms (middle-size open circles in (a)) make triangles together, and their remaining valence electrons make covalent bonding with Ag atoms (large grey circles) [32], leaving no dangling bonds on the surface. The atomic arrangement of Ag is called "hexagonally chained triangle" structure [32], which is one of the Kagome lattices [33]. Its surface-state band is known, from experiments as well as the first-principles calculation, to be parabolic in dispersion and partially filled, resulting in the Fermi level (E_F) crossing [34-36];

$$E = \frac{\hbar^2}{2m*} k_{//}^{\ 2}, \qquad \ldots(1)$$

where E is the electron energy, $k_{//}$ is the in-plane wavenumber of surface-state electrons, m^* is its effective mass, and $\hbar$ is the reduced Planck's constant. Fig. 3(b) is the band dispersion of the Si(111)-$\sqrt{3} \times \sqrt{3}$-Ag surface (with additional Au of 0.01 ML deposition on it) measured by angle-resolved photoemission spectroscopy (ARPES) [37]. This means that the surface-state electrons behave as 2D free electrons along the surface ("Schrödinger electrons").

By depositing tiny amounts of monovalent adatoms such as Au or Ag on the Si(111)-$\sqrt{3} \times \sqrt{3}$-Ag surface, the surface-state band shifts downward with respect to E_F, as shown in Figs. 3(c)(d) [37]. The Ag adatoms can be visualized by scanning tunneling microscopy (STM) images (e) [38]; the adatoms are frozen at low temperature while they are highly mobile at room temperature. The downward shift of surface-state band (c)(d) by adsorption of additional Au atoms means carrier doping into the surface-state band from the adatoms. Then, the electrical resistance of the whole crystal decreases abruptly by depositing Ag adatoms of only 0.01 monolayer (ML) as shown in (f), while the resistance recovers by interrupting the deposition [1,39]. This is because the Ag adatoms gather to nucleate and form Ag clusters, ceasing the carrier doping effect (insets in (f)) when Ag adatom density

exceeds a critical density (*ca*. 0.03 ML in this case). This change in resistance caused by adatom adsorption was the first example to show the electrical conduction through a surface-state band, "*surface-state conduction*"; it had been naively believed that the surface states were so thin compared to the bulk states of underlying 3D substrate and might be cut off by atomic steps on the surface so that it was impossible to detect the surface-state conduction. But the change in resistance shown in Fig. 3(f) by "surface carrier doping" has turned out to be a clear evidence of the surface-state electrical conduction [39]. It was supported by investigating the change in bending of the bulk bands below the surface that the resistance drops observed here were not due to the surface space-charge layer conduction [39]. Surface-state electrical conduction is important especially topological insulators because of their metallic and high conductivity, as seen in the following sections.

Dirac-electrons states

By heating a SiC(0001) crystal around 1550℃ in vacuum or in Ar-gas atmosphere, Si atoms preferentially desorb from the crystal surface, leaving C atoms to form graphene layers on the surface (thermal decomposition method). Figs. 4(a)-(c) show cross sectional TEM (transmission electron microscopy) images of mono-layer graphene (a), bi-layer graphene (b), and tri-layer graphene (c), respectively [40]. The mono-layer graphene shows linear band dispersion or so-called "Dirac cone", as shown in Fig. 4(d) [23],

$$E = \pm \hbar v_F k_{//}, \qquad \ldots(2)$$

where v_F is the Fermi velocity. This relation is obtained by assuming a zero-mass free electron in Dirac equation (so-called "massless Dirac electrons"). The Dirac-cone surface state is formed within the band gap of SiC substrate. It is shown that the Dirac electrons exhibit (half-integer) quantum Hall effect at low temperatures [9,10] and even at room temperature [41]. This highlights the novelty of the massless Dirac electrons to be robust with little scattering, compared to Schrödinger electrons.

A bi-layer graphene, on one hand, in which two graphene layers are stacked in AB sequence (Bernal stacking), shows parabolic bands as shown in Fig. 4(e) [42], meaning the Schrödinger electrons' feature. It is known that the AA-stacking bi-layer graphene shows Dirac electrons' feature [43]. The Dirac-electrons state has non-zero Berry phase, while the Schrödinger-electrons state has zero Berry phase [44]. A "twisted" bi-layer graphene in

which two Graphene layers are stacked with a small rotation angle with each other, shows a flat band around E_F [45]. The dispersion of bi-layer Graphene is very sensitive to the stacking sequence structure.

We can insert (intercalate) foreign atoms and even molecules into spaces between graphene layers, which is similar to graphite-intercalation compounds (GICs) in bulk graphite. It is well known that anodes in Li-ion batteries are graphite in which Li ions are intercalated and de-intercalated for charging and discharging of the battery [46]. For example, Li and Ca atoms are intercalated into a mono-layer graphene (Fig. 4(f)) to make it into a bi-layer graphene by terminating SiC substrate surface with the intercalant atoms (Fig. 4(g)); the buffer layer, which exists below the mono-layer graphene and is tightly bonded to the SiC substrate (Fig. 4(f)), is released from the substrate to be a new graphene layer by terminating the SiC substrate with Li/Ca atoms, resulting in bi-layer graphene (Fig. 4(g)) [47,48]. The Li-intercalation procedure into monolayer and bilayer graphene was observed in real time by low-energy electron microscopy, revealing the stacking-dependent intercalation process and networks of un-intercalated domain walls [49].

When the resistance of the samples was measured in ultrahigh vacuum (UHV) to avoid surface contamination/oxidation, only the Ca-intercalated bi-layer graphene showed superconductivity at ca. 4.5 K, while the pristine graphene and Li-intercalated bi-layer graphene did not (Fig. 4(h)) [42,47]. This is due to carrier doping into the electronic states of graphene from the intercalant atoms though the band structure is complicated due to hybridization of several different states; an interlayer band and saddle-point states, not the Dirac-cone states, can be responsible for the superconductivity. The twisted bi-layer graphene also shows superconductivity [50], which is believed to come from the Mott physics due to the flat band around E_F [45]. These superconductors are being discussed for possible unconventional superconductivity.

4. Symmetry Breaking at Surfaces and Interfaces

Symmetry breaking seriously affects the electronic structures of crystals and their boundaries. We discuss here two kinds of symmetry, time-reversal symmetry (TRS) and space-inversion symmetry (SIS), which are important in condensed matter physics.

Time-reversal operation reverses both the wave (or momentum) vector $\boldsymbol{k}$ and spin

of an electron (Fig. 5(a)). Under no magnetic field and no magnetic order in the materials, the TRS is kept, meaning that the time-reversed electron has the same energy as the original electron;

$$E(\boldsymbol{k},\uparrow) = E(-\boldsymbol{k},\downarrow) \quad \ldots.(3)$$

where $\uparrow\downarrow$ indicate the spin of electron.

On the other hand, by the space-inversion operation in which the (x, y, z) coordinate is transformed into $(-x, -y, -z)$ coordinate, only the wavevector $\boldsymbol{k}$ is reversed while the spin remains unchanged (Fig. 5(b)), because the former is a polar vector and the latter is an axial vector. Inside centrosymmetric crystals such as simple cubic lattices, body/face-centered cubic lattices, and diamond lattices, the SIS is kept, meaning that space-inverted electron has the same energy as the original electron;

$$E(\boldsymbol{k},\uparrow) = E(-\boldsymbol{k},\uparrow) \quad \ldots.(4)$$

Inside non-magnetic and centrosymmetric crystals, both TRS (Eq. (3)) and SIS (Eq. (4)) are fulfilled simultaneously, resulting in

$$E(\boldsymbol{k},\uparrow) = E(\boldsymbol{k},\downarrow). \quad \ldots.(5)$$

This is nothing but spin degeneracy (Kramers' degeneracy), saying that the energy of electrons having the same $\boldsymbol{k}$ does not depend on the spin direction.

On surfaces of any crystals, however, one can notice that SIS is always broken down. It may be easy to imagine that the potential distribution *inside* a centrosymmetric crystal such as schematically drawn in Fig. 6(b) does not change by the space-inversion operation, i.e., reversing upside down and left-right. But when looking at the surface of the crystal, one may notice that the situation is upside down by the space-inversion operation; the vacuum is below the crystal by the operation. This means something is reversed; it is an electric field. The surfaces of any materials always have the surface-normal electric field because, as shown in Fig. 6(a), there exist a potential difference between outside (vacuum level) and inside of the crystal (Fermi level), which corresponds to the work function of material; the inside of the crystal is lower in potential for electrons compared with outside. Then, a potential gradient exists, connecting smoothly the vacuum level outside with the Fermi level inside the crystal, which is nothing but the electric field normal to the surface. The electric field in general breaks down SIS because the electric field vector is reversed by the space-inversion operation. Therefore, the SIS is always broken down at surfaces of any crystals;

the surface-state electrons are localized or moving around at the very asymmetric interface between the crystal and vacuum. Therefore, Eq. (4) and then Eq. (5) are not fulfilled for the surface-state electrons. The spin degeneracy is then lifted, or spin-splitting occurs for the surface-state electrons even for non-magnetic and centrosymmetric crystals. This is called by "Bychkov-Rashba effect" or Rashba effect in short [51,52].

The difference in electrostatic potential between the outside and inside of the crystal mentioned above can be mimicked by a parallel-plate capacitor (Fig. 6(c)), in which the anode is laid just below the surface in the crystal representing lower electrostatic potential and the cathode is on the vacuum side for representing higher potential in vacuum as shown in (a). Then, the surface-state electrons move along the surface in the electric field in the capacitor (Fig. 6(d)). This is a view of the "laboratory system" in which the capacitor is at rest. By transforming the view to the "rest frame of electron" (Fig. 6(e)), the surface-state electron is at rest sitting in the center while the capacitor moves along the crystal surface in the direction opposite to the electron's motion at the laboratory system. This can be regarded as electric charges on the anode/cathode moving, which correspond to electric currents flowing in the opposite directions between outside and inside the crystal (Fig. 6(f)). Such electric currents produce the magnetic field which is perpendicular to the direction of surface-state electron's motion in Fig. 6(d), which is also parallel to the surface of crystal in (b). This magnetic field, which is not a real one but a virtual (or emerging) one, is felt by the surface-state electron only, so that the spin of the electron aligns along this virtual magnetic field. Depending on the direction of spin, parallel or anti-parallel to the virtual magnetic field, the energy of electron is different, or splits into two energy levels, much like Zeeman splitting by a real magnetic field. This is a qualitative understanding of Rashba effect at crystal surfaces in which the energy of surface-state electrons is split depending on the spin direction even under no magnetic field applied.

As one can understand from Figs. 6(d)-(f), the spin direction is always in-plane (parallel to the crystal surface) and perpendicular to the electron momentum (so-called "spin-momentum locking"). In this way, the (orbital) motion of electron in an electric field (Fig. 6(d)) and the electron's spin "interact" with each other (through the virtual magnetic field), resulting in the energy-level splitting. This is "spin-orbit interaction" (SOI).

A non-relativistic approximation of Dirac Hamiltonian for an electron leads to a so-

called Rashba Hamiltonian;

$$H = \frac{\hbar^2}{2m^*}\boldsymbol{k}^2 + V + \frac{e\hbar^2}{4m^{*2}c^2}\boldsymbol{\sigma}\cdot(\mathrm{grad}\,V \times \boldsymbol{k}), \quad \ldots(6)$$

where $\boldsymbol{k}$ is the wavevector of electron (having the in-plane components, k_x and k_y only, because of the surface-state electron considered), m^* is the effective mass, $\boldsymbol{\sigma}$ is the Pauli spin operator of electron, and V is the electrostatic potential. The potential gradient grad V is the surface-normal (z-direction) electric field as described in Figs. 6(a)(c). The term $(\mathrm{grad}\,V \times \boldsymbol{k})$ represents the virtual magnetic field (Fig. 6(f)), which is parallel to the crystal surface and perpendicular to $\boldsymbol{k}$. The inner product between $\boldsymbol{\sigma}$ and $(\mathrm{grad}\,V \times \boldsymbol{k})$ means the SOI.

The eigenenergy of this Hamiltonian is (by neglecting a constant value for energy reference)

$$E(k) = \frac{\hbar^2 k^2}{2m^*} \pm \alpha k = \frac{\hbar^2}{2m^*}(k \pm k_{SO})^2 - \Delta_{SO}, \quad \ldots(7)$$

where the so-called Rashba parameter $\alpha \equiv \frac{e\hbar^2 E_0}{4m^{*2}c^2}$ with $E_0 \equiv |\mathrm{grad}\,V|$, $k_{SO} \equiv \frac{\alpha m^*}{\hbar^2}$, $\Delta_{SO} \equiv \left(\frac{\alpha m^*}{\hbar^2}\right)^2$, and $k \equiv |\boldsymbol{k}|$. The double sign in Eq. (7) is due to two directions of spin, parallel and anti-parallel to the virtual magnetic field, respectively, meaning the energy splitting. The energy splitting is larger for larger α value, or larger E_0, i.e., larger degree of asymmetry in the potential distribution at the surface. But, in the framework of 2D free electron model for the surface-state electrons, the work function of usual materials produces $E_0 \sim 1$ eV/Å, resulting in a very small Rashba parameter $\alpha \sim 10^{-6}$ eVÅ, which is much smaller than experimental values $\alpha \sim 0.2$ eVÅ. In real materials, E_0 is the largest near ion cores of respective atoms on the crystal surface. The Rashba parameter α is written quantum-mechanically by a volume integral

$$\alpha \propto \int E_0 \cdot |\psi|^2 dV \quad \ldots(8)$$

where the wavefunction ψ of the surface-state electron should be asymmetric near the ion core [53]. Then, larger E_0 around the ion cores of heavier (larger atomic-number) atoms produces a larger Rashba parameter and then the larger Rashba energy splitting. This "atomic SOI" by heavy atoms on the topmost layer of crystal surfaces makes Rashba splitting larger. Actually, adsorption of monolayer of heavy metal atoms on semiconductor surfaces, such as Au/Si(111), Tl/Ge(111), Ti/Si(111) systems, shows $\alpha \sim 0.2$ eVÅ, and

Bi/Ge(111) shows a value as large as $\alpha \sim 1.8$ eVÅ. This α value of Bi/Ge(111) system is approximately twice as large as that of the surface of bulk Bi crystal. This is because, according to Eq. (8), the Rashba energy splitting depends also on the degree of asymmetry of the surface-state electron wavefunction along z direction [53,54].

5. Spin-splitting surface state (1) —Surface Rashba Systems—

Equation (7) indicates that a parabolic band dispersion of free electrons Eq. (1), for example, splits into two bands by shifting the band along $\boldsymbol{k}$ axis as shown in Fig. 7(a); the blue band is for electrons having spin pointing in $+y$ direction, while the red band is for electrons having spin in $-y$ direction, because the horizontal axis in Fig. 7(a) is k_x. This is the Rashba effect. This is in sharp contrast with the Zeeman effect under applied magnetic field in which the band splits into two by shifting the band along the energy E axis.

The Fermi surface also splits into two on (k_x, k_y) plane by the Rashba effect as shown in Fig. 7(b). The spins of Fermi electrons are shown by short arrows which are always perpendicular to the momenta of respective electrons; the spins are aligned in tangential directions of the Fermi surface clockwise or counterclockwise; the inner and outer Fermi surfaces are for electrons having opposite directions of spin.

Figure 7(c) shows experimental results of band dispersion of Au(111) surface states measured by spin- and angle-resolved photoemission spectroscopy (SARPES) [55]. Two parabolic bands with different colors are observed, which are shifted from each other along k_x-axis; the bule and red indicate the spin polarization of photoelectrons in $+y$ and $-y$ directions, respectively. This is exactly what we expect in Fig. 7(a). Although Au is a non-magnetic material, the energy of surface-state electrons depends on the spin direction; compare the energies of red and blue bands with the same wavenumber. The two bands of the opposite spins always degenerate at $k = 0$ (and Brillouin zone boundaries, so-called TRIM, time-reversal-invariant momenta) because of the time-reversal symmetry.

By considering the Fermi electrons A-D in Fig. 7(c), one can notice an interesting fact in real space. The electron A moves along $+x$ direction with spin pointing $+y$ direction, while the electron B moves along $-x$ direction with the same wavenumber having spin pointing $-y$ direction (Fig. 7(d)). Therefore, the electrons A and B cancel out

the charge current, while pure spin current remains; since the flow of $-y$ spin along $-x$ direction (electron B) is equivalent to the flow of $+y$ spin along $+x$ direction (electron A) due to the time-reversal symmetry, it means a double flow of $+y$ spin along $+x$ direction. The electrons C and D are also in the same relation, having opposite but the same magnitude of momenta and opposite spins, resulting in no charge current but finite pure spin current. While the spin currents by A/B pair and C/D pair flow in opposite directions and therefore are partially cancelled out with each other, the spin current by A/B pair dominate that by C/D pair because of the larger magnitude of k_x. Though this is the spin current along x direction, the spin current flows in any other directions because of the circular Fermi surfaces (Fig. 7(b)). Thus the Rashba-type surface is an interesting playground for spin current.

Rashba superconductivity

Another example of Rashba surfaces is a monolayer alloy of Tl and Pb on Si(111), showing Si(111)-$\sqrt{3} \times \sqrt{3}$-(Tl,Pb) surface superstructure. As shown in Fig. 8(a), Tl and Pb atoms arrange themselves regularly in a single atomic layer [25]. Its scanning tunneling microscope (STM) image (b) [26] and reflection high-energy electron diffraction (RHEED) pattern (c) indicate a well-ordered structure in long range. Its band dispersion was measured by ARPES (d), which was confirmed by density-functional theory calculation (e) [25,26]. One notices that bands crossing E_F split into two such as those denoted by $\Sigma 1/\Sigma 1'$ and $\Sigma 2/\Sigma 2'$. These are Rashba-slit bands, having opposite spins from each other, due to heavy atoms of Tl and Pb on the topmost surface of crystal.

The Tl+Pb monolayer has turned out to be superconducting around 2.5 K as shown in Fig. 8(f) [26]. This was measured *in situ* by a four-point probe operating in ultrahigh vacuum (UHV) to preserve the monolayer structure without oxidation/contamination [56,57]. This is so-called Rashba superconductivity, which can be beyond the conventional superconductivity of BCS theory because the BCS theory is based on spin degeneracy.

Let us consider first superconductivity of spin-degenerate systems; two electrons, A and B, at E_F have opposite wavevectors $+\boldsymbol{k}$ and $-\boldsymbol{k}$, each of which has two spin states, $\uparrow$ *and* $\downarrow$, with the same energy; $|+\boldsymbol{k}\uparrow\rangle_A$ or $|+\boldsymbol{k}\downarrow\rangle_A$, and $|-\boldsymbol{k}\uparrow\rangle_B$ or $|-\boldsymbol{k}\downarrow\rangle_B$. When

they make Cooper pairs to be superconducting, the wavefunctions of Cooper pairs are

$$\text{Spin-singlet} \quad |\boldsymbol{k}\uparrow\rangle_A|-\boldsymbol{k}\downarrow\rangle_B - |\boldsymbol{k}\downarrow\rangle_A|-\boldsymbol{k}\uparrow\rangle_B \quad \ldots(9)$$

$$\text{Spin-triplet} \quad |\boldsymbol{k}\uparrow\rangle_A|-\boldsymbol{k}\downarrow\rangle_B + |\boldsymbol{k}\downarrow\rangle_A|-\boldsymbol{k}\uparrow\rangle_B \quad \ldots(10)$$

$$|\boldsymbol{k}\uparrow\rangle_A|-\boldsymbol{k}\uparrow\rangle_B,\ |\boldsymbol{k}\downarrow\rangle_A|-\boldsymbol{k}\downarrow\rangle_B.$$

By exchanging the two electrons A and B with each other in the momentum space, i.e., exchanging $+\boldsymbol{k}$ and $-\boldsymbol{k}$, Eq. (9) shows a sign change (odd parity) while Eq. (10) does not change its sign (even parity). Thus, the parity of wavefunction of Cooper pairs is either odd or even in BCS superconductors.

On the Rashba-split Fermi surface in Fig. 7(b), on the other hand, the electrons A and B are $|\boldsymbol{k}\uparrow\rangle_A$ and $|-\boldsymbol{k}\downarrow\rangle_B$, respectively on the outer Fermi circle, without spin-opposite states such as $|\boldsymbol{k}\downarrow\rangle_A$ and $|-\boldsymbol{k}\uparrow\rangle_B$. Therefore, the Cooper pair may be

$$|\boldsymbol{k}\uparrow\rangle_A|-\boldsymbol{k}\downarrow\rangle_B. \quad \ldots.(11)$$

By exchanging the two electrons, the state changes into $|-\boldsymbol{k}\uparrow\rangle_B|\boldsymbol{k}\downarrow\rangle_A$, which is totally different from Eq. (11), and does not exist on the outer Fermi circle in Fig. 7(b). Therefore, the wavefunction of Eq. (11) is neither odd-parity nor even-parity. Then, Eq. (11) can be re-written by adding/subtracting a virtual state $|\boldsymbol{k}\downarrow\rangle_A|-\boldsymbol{k}\uparrow\rangle_B$ as

$$|\boldsymbol{k}\uparrow\rangle_A|-\boldsymbol{k}\downarrow\rangle_B$$

$$= \frac{1}{2}(|\boldsymbol{k}\uparrow\rangle_A|-\boldsymbol{k}\downarrow\rangle_B - |\boldsymbol{k}\downarrow\rangle_A|-\boldsymbol{k}\uparrow\rangle_B) + \frac{1}{2}(|\boldsymbol{k}\uparrow\rangle_A|-\boldsymbol{k}\downarrow\rangle_B + |\boldsymbol{k}\downarrow\rangle_A|-\boldsymbol{k}\uparrow\rangle_B) \quad \ldots(12)$$

The first two terms are the same as Eq. (9), and the last two terms are Eq. (10), meaning that the state of Eq. (11) is a mixture of spin-single and spin-triplet states. In other words, odd- and even-parity states of Cooper pairs are mixed. Thus, the superconductivity in the Rashba-spin-split system is parity-broken superconductivity, which is not described by the BCS theory.

If two electrons, A and C, or B and D on the Fermi surface in Fig. 7(b), make Cooper pairs, the center of mass of a Cooper pairs has a finite momentum because of different magnitudes of momentum of the two electrons. This is called Fulde–Ferrell–Larkin–Ovchinnikov (FFLO) state of superconductivity [58,59], which is also beyond the BCS framework.

These kinds of unconventional superconductivities are expected to have unique properties such as extremely large critical magnetic field [60], spin-polarized supercurrent [61], topological nature, and so on.

The monolayer Rashba superconductor, Si(111)-$\sqrt{3} \times \sqrt{3}$-(Tl,Pb) surface superstructure, was investigated by low-temperature STM at 0.5 K under magnetic field applied perpendicular to the surface [62]. The color in Figs. 9(a)-(d), dI/dV (conductance) maps, indicates the zero-bias conductance in scanning tunneling spectroscopy (STS) at each point on the surface; darker purple means zero conductance, or zero density of state (DOS) at E_F, meaning a superconducting gap opening, as shown by the STS curve at the bottom in (e), while brighter red means gap filling to diminish the superconducting gap at E_F, as shown by spectra at higher magnetic fields in (e). Under no magnetic field applied (a), the whole surface shows the superconducting gap opening homogeneously, while the surface shows the gap closing homogeneously under high magnetic field of 1.2 T (d). Under the intermediate magnetic field (b)(c), vortexes are observed as bright dots, of which number increases with the field strength. These are normal-state areas where the quantized magnetic flux $h/2e$ for each vortex penetrates (h is Planck's constant and e is the elementary charge). Although Fig. 9(d) looks breakdown of the superconductivity over the whole area (because 1.2 T is larger than the upper critical magnetic field obtained by transport measurement [26]), a small dip is observed in the STS spectrum at 1.2 T in (e). Although such a so-called pseudo-gap can be a sign of an unconventional superconductivity, conclusive evidence for the unconventionality is not yet found [63].

6. Spin-splitting surface state (2) —Topological Insulators—

Band inversion

The Rashba effect described by a Hamiltonian Eq. (6) is due to SOI by the potential gradient normal to the crystal surface as depicted in Fig. 6. And as mentioned in Section 4, the potential gradient around ion cores of atoms on the crystal surface, $grad\ V = \frac{\boldsymbol{r}}{r}\frac{dV}{dr}$ for cases of centrosymmetric potential, are also important for large Rashba effect due to "atomic SOI". Then, the Rashba term in Eq. (6) is re-written by

$$\frac{e\hbar^2}{4m^{*2}c^2}\boldsymbol{\sigma} \cdot (\mathrm{grad}\, V \times \boldsymbol{k}) = \frac{e}{2m^{*2}c^2}\frac{1}{r}\frac{dV}{dr}\,\boldsymbol{s}\cdot\boldsymbol{\ell} \ ,$$

where $\boldsymbol{s}$ is the spin $\boldsymbol{s} = \hbar\boldsymbol{\sigma}/2$ and $\boldsymbol{\ell}$ is the angular momentum of the electron moving around the ion core of each atom in the crystal lattice. This also indicates that the energy-

level split and shift depend on the atomic orbitals, s-orbital ($\ell = 0$), p-orbital ($\ell = 1$), d-orbital ($\ell = 2$),….

In case of non-centrosymmetric crystal structures in which SIS is broken down even inside the 3D bulk crystals, such effect leads to changes in bulk band energy. Then, in some materials, the top of the bulk valence band goes up and the bottom of the bulk conduction band goes down in energy due to different orbital components of the respective bands and opposite spins (Figs. 10(a)(b)). When the SOI is strong enough, it leads to an inversion of energy positions between the top of valence band and the bottom of conduction band; the two bands intersect with each other (Fig. 10(b)). Then, an energy gap opens again (sometimes called a "negative band gap" or "non-trivial gap"), as schematically shown in Fig. 10(c), with the band characters at the inverted-band regions taken in the opposite bands. This kind of materials having band inversion is called topologically non-trivial and topological insulators. Though the "negative band gap" between the inverted bands is usually as small as less than 1 eV like semiconductors, it is a custom to call them insulators.

This band inversion results in parity mixing in the wavefunction in the respective bands. Usually, the valence band originates from a bonding state between atoms in the crystal lattice, having even-parity wavefunction, while the conduction band originates from an anti-bonding state composed of odd-parity wavefunction. Then, the inverted-band regions in topological insulators have opposite parity to those in the other regions of the same bands. In this way, the nature of wavefunction of band electrons changes locally in the momentum space (Fig. 10(c)), which is in sharp contrast to trivial insulators/semiconductors in Fig. 10(a). It is impossible to distinguish non-trivial insulators from trivial ones just by the band dispersion nor the size of band gap; we need to investigate the parity of wavefunctions at several (TRIM) points in Brillouin zone.

This kind of changes in the wavefunction due to band inversion is described by Berry phase; the phase of electron wavefunction $\psi(\boldsymbol{k})$ changes locally by π at the inverted-band region in a band due to Berry curvature, as schematically shown in Fig. 10(e), while trivial insulators have no Berry phase in a band (Fig. 10(d)). The Berry phase γ is defined by a path integral of "Berry connection" $\boldsymbol{A}(\boldsymbol{k})$ around a closed loop C in Brillouin zone [5,6];

$$\gamma = \oint_C d\boldsymbol{k} \cdot \boldsymbol{A}(\boldsymbol{k}), \text{ where } \boldsymbol{A}(\boldsymbol{k}) = i\left\langle \psi(\boldsymbol{k}) \middle| \frac{\partial}{\partial \boldsymbol{k}} \middle| \psi(\boldsymbol{k}) \right\rangle. \quad \ldots(13)$$

$\boldsymbol{A}(\boldsymbol{k})$ is a kind of curvature of the wavefunction of electrons in a band (not a curvature of band dispersion) in the momentum space, which is non-zero around the band-inverted region. With the Berry connection $\boldsymbol{A}(\boldsymbol{k})$, the Berry curvature $\boldsymbol{B}(\boldsymbol{k})$ is defined by

$$\boldsymbol{B}(\boldsymbol{k}) = \boldsymbol{\nabla}_{\boldsymbol{k}} \times \boldsymbol{A}(\boldsymbol{k}). \quad \ldots(14)$$

Then, the Berry phase is re-written, according to Stokes Theorem, by an area integral of $\boldsymbol{B}(\boldsymbol{k})$ over the area S_C enclosed by the loop C;

$$\gamma = \oint_C d\boldsymbol{k} \cdot \boldsymbol{A}(\boldsymbol{k}) = \iint_{S_C} dS \cdot \boldsymbol{B}(\boldsymbol{k}). \quad \ldots(15)$$

Here again, a similarity is arisen between real magnetic field in real space and virtual magnetic field in momentum space. When we regard $\boldsymbol{A}(\boldsymbol{k})$ as a "virtual vector potential", $\boldsymbol{B}(\boldsymbol{k})$ in Eq. (14) is a "virtual magnetic field". Then, according to Eq. (15), the Berry phase γ can be regarded as a "virtual magnetic flux" penetrating the closed loop *C* in momentum space. When the loop *C* surrounds the band-inverted region in the momentum space (see Fig. 10(f)), the virtual magnetic flux penetrates the loop *C*. Then, we can say that the phase of wavefunction is changed due to this virtual magnetic field in momentum space, much like Aharonov-Bohm effect (AB effect) in real space [64]. The AB phase of the wavefunction acquired by the vector potential in real space and the Berry phase in momentum space are collectively called by "geometrical phase", which are distinct from the dynamical phase of wavefunction related with wave propagation.

The band inversion and the accompanying continuous changes in phase of the wavefunction in a band are symbolized by a Möbius strip (Fig. 10(c)) where the two sides of strip are continuously connected with each other. Trivial insulators, on one hand, correspond to a simply connected strip (Fig. 10(a)) where the two sides are clearly distinguished. Therefore, the name of "topological" represents well the substance of physics here.

Topological surface states

What happen at the crystal surface of such a topological insulator? Vacuum outside the material is a kind of trivial insulator (Fig. 10(a)); the Dirac sea, filled with electrons having negative energy, is a kind of valence band, while vacuum in the positive energy side is a kind of conduction band, in between an energy gap of 1.022 MeV exits which corresponds to energy of electron-positron pair creation. This is much like a semiconductor

in which electron-hole pair creation occurs in the conduction and valence bands across the band gap. Therefore, the surface of a topological insulator crystal is an interface between a non-band-inverted region (Fig. 10(a)) and a band-inverted region (Fig. 10(c)). Therefore, at the surface of a topological insulator, the conduction and valence bands remain crossing as shown in Fig. 10(b), leaving metallic states without an energy gap. The surface states of topological insulators are thus always metallic, usually having Dirac-cone-type linear band dispersion, spanning the "negative band gap" of bulk states of a topological insulator, as shown in Fig. 10(f) and Fig. 2(d). In this way, the topological surface states originate from the nature of bulk bands, not from the surface properties (so-called "bulk-boundary correspondence"). Therefore, the topological surface states are robust against surface modifications/degradation.

Bi_2Se_3 and Bi_2Te_3 are typical topological insulators [27], of which crystal structure is schematically shown in Fig. 11(a). A quintuple layer (QL), consisting of Se(Te)-Bi-Se(Te)-Bi-Se(Te) atomic-layer planes, is a unit of stacking along *z*-direction ((111) direction). As shown in a cross-sectional transmission electron microscope (XTEM) image in Fig. 11(b) [65], Bi_2Te_3(111) crystal grows epitaxially on Si(111) substrate even under lattice mismatching with the substrate. This is because the QLs are connected with each other by van der Waals interaction between Se-Se layers ("van der Waals gap"). This is an example of so-called "van der Waals epitaxy" prosed by A. Koma [66], so that we can grow Bi_2Te_3 and Bi_2Se_3 crystals in QL-by-QL manner irrespective of the lattice mismatch with the substrate.

Figures 11(c)(d) shows ARPES images taken from (c) 3QL-thick and (d) 8QL-thick Bi_2Se_3 films grown on Si(111) substrate, respectively [67]. Across the band gap between the conduction and valence bands, a faint feature of Dirac-cone type bands is seen in Fig. 11(d). This is the surface states of Bi_2Se_3 crystal, as schematically shown in Fig. 10(f). According to SARPES [68], two branches of the Dirac-cone-type surface states in Fig. 11(d) has opposite spin polarization to each other. This topological surface state is the same as that for an exfoliated film from a bulk crystal of Bi_2Se_3 [69].

For the 3QL-thick Bi_2Se_3 film in Fig. 11(c), on the other hand, no trace of Dirac cone is seen in the band gap. This is because the film is so thin that the Dirac-cone type topological surface states on the front surface (which is the interface with vacuum) and the back surface

(which is the interface with Si(111) substrate) are overlapped with each other in the film, resulting in hybridization between them and an energy gap opening in the surface-state bands. The wavefunction of the topological surface state is known to penetrate the bulk by about 2 QL thick below the surface [70] so that the 3QL-thick Bi_2Se_3 film is thin enough for the surface states of the front and back surfaces to overlap with each other. Because of this hybridization gap, there are no metallic states in the bulk band gap in Fig. 11(c). In other words, the hybridization means that, because of its robustness, the topological surface (interface) state at the back surface of the film survives even under the contact with Si substrate.

Electrical transport at Dirac-cone surface states

There is one more thing to be pointed out for real crystals of topological insulators. The inner bulk of real crystals of topological insulators is not really insulating due to some lattice defects such as deficit of chalcogen atoms, which makes the Fermi level crossing the bulk conduction band as shown by Bi_2Se_3 case in Figs. 11(c)(d). Then, electrical conduction occurs not only through the surface-state bands, but also through the bulk bands, which prevents us from detecting interesting properties of surface-state transport such as spin-dependent transport.

Figure 12(a) shows ARPES results of the Fermi surface (upper panel) and band dispersion (lower panel) near the Fermi level (E_F) of 3QL-thick Bi_2Te_3 film grown on Si(111) substrate [71]. The Fermi surfaces and bands denoted by B and S are the bulk conduction band and Dirac-cone-type surface-state bands, respectively. Because the penetration depth of the surface-state wavefunction at Bi_2Te_3 crystal is only one QL [72], the hybridization of the surface-state wavefunction between the front and back surfaces of film (as seen at Bi_2Ee_3 film in Fig. 11(c)) does not occurs even at 3QL thick film.] Since the bottom of the bulk conduction band B is below E_F in Fig. 12(a), the inner bulk is not insulating, rather a "*n*-type degenerate semiconductor" as in Bi_2Se_3 case shown in Fig. 11. To make the bulk insulating, we doped holes by incorporating Pb atoms during the growth of Bi_2Te_3 films. As shown in Figs. 12(b)-(f), by increasing the Pb-atom concentration, the bulk conduction band B as well as the surface-state band S go up with respect to E_F, resulting in bulk-insulating state around 14% concentration of Pb atoms (e) in which the bulk band B is above E_F so that E_F crosses

the surface-state band S only.

From the size of the Fermi circles in the upper panels of (a)-(f) in Fig. 12, we can estimate the carrier densities at E_F in the bulk states (inner Fermi circle) and in the surface states (outer Fermi circle) separately as a function of the Pb concentration, as shown in Fig. 12(g). It indicates that the bulk carriers (blue points) disappear above 10%-Pb concentration and only the surface-state carriers (red points) remain there. The sheet (2D) conductivity of these thin-film samples was measured at room temperature *in situ* in UHV by micro-four-point probe method [57], the results of which are shown in Fig. 12(h). The conductivity (blue points) remains constant around 20 μS above 10%-Pb concentration; this is the conductivity originating from the topological surface state only, because the contribution of bulk states to conductivity is negligible. Although, in this way, we could detect the surface-state conduction with help of ARPES data, the carrier mobility (around 30 cm^2/Vs) was not so high as expected , which was calculated by Drude model using the carrier density in Fig. 12(g); this mobility is only twice as in the surface-state transport of a trivial material Si(111)-$\sqrt{3} \times \sqrt{3}$-Ag surface structure [39]. Although a very high carrier mobility is expected due to the linear dispersion of Dirac-cone type surface state, carrier scattering by Pb atoms and other defects degrades the property in real crystals; scattering of the surface-state electrons into the bulk bands may occur at room temperature because of the small band gap of Bi_2Te_3.

The electrical conductivity of topological surface states of Bi_2Te_2Se crystal, which has a wider band gap in the bulk band structure, was detected and measured by variable probe-spacing method using micro-four-point probes [73], showing that the mobility was around 390 cm^2/Vs, a much higher than that of Bi_2Te_3 in Fig. 12, probably due to fewer defect scattering and the wider bulk band gap [74]. By tuning the growth condition for epitaxial growth of Bi_2Te_3 films to reduce the defect density, another group obtained metallic temperature dependence of the film conductivity, meaning a surface-state dominated electrical conduction [75]. It produced a further higher mobility 4600 cm^2/Vs. This is exceptional high for surface-state electrons, a signature of unique property of Dirac-cone-type topological surface states. This series of measurements means that the carriers in topological surface states are scattered by defects as in trivial surface states even though the spin-momentum locking works mentioned below; the scattering angles are not restricted to be 180° in 2D surface states.

Helical Dirac-cone surface states

The Dirac-cone-type topological surface state has a unique feature of spin polarization, as depicted in Fig. 13(a) and also the Fermi surface in Fig. 13(b). As in the case of Rashba systems, the spin-momentum locking works also for topological surface states because of the strong SOI; the spin $\boldsymbol{s}$ (short thick arrows in Fig. 13) is always perpendicular to the momentum $\boldsymbol{k}$ (long thin arrows). This means that the 180° back scattering is inevitably accompanied with spin flip. In other words, the 180° back scattering is prohibited in non-magnetic topological insulators because of no magnetic impurities which cause spin flip. But scattering with other angles can occur with some probability in 2D surface states.

Another interesting consequence of the spin-momentum locking is pure spin current. The Fermi surface here (Fig. 13(b)) is only one of the two Fermi circles in Fig. 7(b) for the Rashba systems. This means that, in real space as shown in Fig. 13(c), pure spin current flows on the surfaces of a topological insulator, without cancellation by another Fermi circle in case of Rashba systems in Fig. 7(d). Therefore, stronger pure spin current flows on topological insulators' surfaces than on Rashba surfaces. Detection of such spin-dependent transport on the surfaces is an interesting and important challenge.

In 2D topological insulators (sometimes called as quantum spin Hall insulators), as in Fig. 13(d), the interior of the surface area is insulating while the edge is metallic where electrons with opposite spins flow in opposite directions, producing pure spin current flowing along the edge. The two flows of electrons with opposite directions and opposite spins at the edges never merge because $180°$-degree back scattering (by non-magnetic impurities) never occur at the edges due to the spin-momentum locking. Scatterings with angles other than $0°$ (forward scattering) and $180°$ (back scattering) never occur in 1D edge channels. Since pure spin current does not carry charge, no energy dissipation occurs, meaning that pure spin current at the edges can be a dissipation-less information carrier. The quantum spin Hall insulator state was first confirmed experimentally with a HgTe thin layer sandwiched between CdTe layers [76]. Under the band-inversion condition with E_F tuned within the inverted band gap, its longitudinal conductance is exactly a quantized value $2\,e^2/h$ which originates from one of the opposite-spin flows in the edge channels on both

sides of sample. This value is identical irrespective of the sizes of samples. The topological nature in transport is clear in case of 1D edge channels, rather than 2D surface states. An interesting idea is proposed to make the current flow with the same spin direction on both edges in 2D TI; it is just to bend a 2D TI into a half cylinder [77].

7. Photo-Galvanic Effect due to spin-momentum locking

In solar cells made of trivial semiconductors, we need *pn* junction to make photocurrent flow in one direction (non-reciprocal current) in which a potential slope at the junction induces one-way photocurrent. On the other hand, spin-split surface-state bands on the Rashba systems and topological insulators are useful to produce such non-reciprocal photocurrent, even without *pn* junction. Since the circularly polarized light has spin angular momentum ($s = \pm 1$), it can be transferred to electrons on/in the materials via spin-selective optical excitations between spin-split bands. Such spin-selective excitations occur asymmetrically with respect to Γ point ($k = 0$) in the momentum space; as shown in Fig. 14(a) for helical Dirac-cone type surface states of topological insulators, excitations from the state A of spin $s_x = +1/2$ to the state B of spin $s_x = -1/2$ occur on $k_y > 0$ side in the momentum space, producing photocurrent flowing in $+y$ direction in real space, while the excitations from A' ($s_x = -1/2$) to B' ($s_x = +1/2$) states occur on $k_y < 0$ side, producing photocurrent flowing in the opposite direction. The former excitation is induced by e.g., right-handed circularly polarized (RCP) light ($s = -1$), while the latter is by left-handed circularly polarized (LCP) light ($s = +1$) due to conservation of angular momentum at the excitation. We can expect in this way the helicity-dependent photocurrent on topological insulators.

This process is also understood by a shift of the Fermi surface as shown in Fig. 14(b). By injecting electrons having spin $s_x = -1/2$ into the electron system by optical excitation, electrons B having $s_x = -1/2$ are larger in number density than electrons B' having $s_x = +1/2$, which is equivalent to a shift of the Fermi surface towards positive k_y direction, meaning photocurrent flowing in $+y$ direction in real space. Since the momentum and spin of an electron are so strongly coupled in this way due to the spin-momentum locking that the injection of one-direction spin produces electrical current flowing in a particular direction. This is called "circular photo-galvanic effect (CPGE)" [78],

which is one of the "inverse Rashba-Edelstein effect" where, in more general, spin injection induces electrical current. This is an inversed process of the direct "Rashba-Edelstein effect" where flow of electrical current along one direction produces spin polarization. These are due to spin-momentum locking by strong SOI.

Figure 14(c) shows our experimental setup to measure the helicity-dependent photocurrent on a thin film of topological insulator Bi_2Se_3 which were epitaxially grown on Si(111) substrate by molecular beam epitaxy (MBE) technique [79]. The photocurrent was measured through clamp electrodes at both ends of the sample, under oblique irradiation of infrared laser light (its wavelength $\lambda = 1550$ nm) (which is for injecting in-plane spin component). By rotating a quarter-wave plate (QWP) installed in the optical path, we can change the polarization of light, linear polarization and right/left-handed circular polarization (LCP and RCP). As shown in Fig. 14(d), the measured photocurrent is changed with rotation of the QWP, in which the polarization of light is schematically shown on the top. Especially, the photocurrent under the LCP light irradiation (indicated by L) is distinctively different from the photocurrent under the RCP light (indicated by R). This is a clear example of non-reciprocal photocurrent on a topological insulator which originates from a mechanism mentioned above, not from a *pn* junction. The potential slope at the *pn* junction in a usual solar cell breaks SIS while the circularly polarized light breaks TRS, both of which produce non-reciprocal current.

The Rashba-type spin-split surface-state bands also produces similar CPGE because similar asymmetric excitations occur with respect to Γ point ($k = 0$) in the momentum space. We have found that the Rashba-type surface Si(111)-$\sqrt{3} \times \sqrt{3}$-(Tl,Pb) shown in Fig. 8 actually shows the CPGE even with the mono-atomic-layer thick system [80]. Although the efficiency for converting light to electric current in the CPGE systems is much lower than in the *pn* junction type solar cells so far, it would be interesting to explore the phenomenon with new quantum materials.

8. Magnetic Topological Insulators

As described in Section 4, spin degeneracy Eq. (5) is lifted, $E(\boldsymbol{k},\uparrow) \neq E(\boldsymbol{k},\downarrow)$, under SIS-broken circumstances with strong SOI. But, looking at the Dirac point in a helical Dirac-

cone-type surface states of topological insulator (Fig. 13(a)), the spin degeneracy occurs $E(\boldsymbol{k}=0,\uparrow)=E(\boldsymbol{k}=0,\downarrow)$, while the other states of $\boldsymbol{k}\neq 0$ are spin-spit $E(\boldsymbol{k},\uparrow)\neq E(\boldsymbol{k},\downarrow)$. On the other hand, by applying magnetic field or by introducing magnetic order in materials, the TRS is broken down, which also lifts the spin degeneracy due to Zeeman effect, even at the Dirac point, resulting in an energy gap opening at the Dirac point ("Dirac gap"), as shown in Fig. 2(e).

We have found an example of such Dirac gap opening by making the surface of a topological insulator ferromagnetic [29]. As described above and shown in Fig. 15(a), the surface state of a crystal of Bi_2Se_3 shows a Dirac-cone type dispersion, without a gap opening at the Dirac point. By depositing MnSe onto this crystal of Bi_2Se_3 at elevated temperature, MnSe atomic layer is incorporated in the middle of the topmost quintuple layer of Bi_2Se_3 crystal unit cell as shown by a schematic of atomic-layer stacking structure in Fig. 15(b) (left), forming a septuple layer $MnBi_2Se_4$ (Se-Bi-Se-Mn-Se-Bi-Se) on top of the Bi_2Se_3 crystal. Since the spins of Mn atoms are aligned in surface-normal direction, this makes the surface layer ferromagnetic, showing magnetic hysteresis [29]. ARPES measurements show a gap opening at the Dirac point (sometimes called "massive" Dirac cone) in the $MnBi_2Se_4/Bi_2Se_3$ heterostructure as shown in Fig. 15(b) (middle), which is in contract with (massless) Dirac cone of Bi_2Se_3 in Fig. 15(a) (middle). Such an introduction of magnetic order makes the Dirac cone "chiral" in which spins of electrons at the upper and lower edges at the Dirac gap point opposite (due to Zeeman effect), as illustrated in Fig. 15(b)(righ). It is known that when the Fermi level is tuned in the Dirac gap, the interior of the surface is insulating while the edge of the surface is metallic due to a "chiral edge state" in which electrical current flows in one direction along the edge without energy dissipation, much like in the state of quantum Hall effect. Such a chiral edge state is shown by one-side band across the Dirac gap as shown in Fig. 2(e). This is called as "quantum anomalous Hall effect (QAHE)", which is lower-dimensional version of 3D topological insulators with metallic 2D surface-state bands hosting dissipation-less spin current in their surfaces; the 2D surface is an "edge" of a 3D crystal. The 1D metallic edge state in the QAHE is an "edge" of the "gapped" 2D topological surface.

The QAHE was first observed on a magnetic topological insulator made of random doping of magnetic impurities [81] and later on modulation-magnetic-doping topological

insulators [82] and also on the intrinsic ferromagnetic topological insulator $MnBi_2Te_4$ [83]. The dissipation-less chiral-edge electrical current at QAHE (a schematic in Fig. 15(b)) as well as dissipation-less helical-edge pure spin current flowing at the 2D topological insulator (Fig. 13(d)) look very attractive for application to ultra-low power-consumption electronics.

Ferromagnetic topological insulators are platforms for other interesting phenomena such as formation of magnetic skyrmions [84]. Skyrmions are isolated excitations in spin systems having spiral and non-collinear spin arrangements, behaving stably as particles characterized by topological quantum numbers. Skyrmions, or in more general non-collinear spin arrangements, are induced by Dzyaloshinskii–Moriya interaction (DMI) [85,86] or antisymmetric exchange interaction which is effective under broken SIS circumstances such as on crystal surfaces and in thins films on substrates. An example is shown in Fig. 16(a) in which a thin layer of topological insulator $(Bi,Sb)_2Te_3$ is sandwiched between thin layers of a ferromagnetic topological insulator $Mn(Bi,Sb)_2Te_4$ [87]. This sandwich heterostructure was grown on Si(111) substrate by MBE technique and confirmed by a scanning transmission electron microscopy image (Fig. 16(b)). $(Bi,Sb)_2Te_3$ and $Mn(Bi,Sb)_2Te_4$ layers have similar atomic stacking structures as Bi_2Te_3 and $MnBi_2Te_4$ shown in Fig. 15; Bi atoms in the lattices are partially replaced by Sb atoms with crystal structures unchanged, which just results in hole doping to tune E_F. The layers are epitaxially grown as shown by RHEED pattern in Fig. 16 (c) [88].

The ferromagnetic layers on both sides of this sandwich-structure film make the Dirac-gap opening in the surface states on both sides. Hall resistance measured at 0.5 K under sweeping magnetic field applied in surface-normal direction exhibits a hysteresis and anomalous Hall effect (Fig. 16(d)), meaning ferromagnetism in the film; the two ferromagnetic layers on both sides magnetically interact with each other (interlayer exchange coupling). Since the Fermi level is not exactly tuned within the Dirac gap, the Hall resistance is far below the quantized value of $h/2e^2$($\cong$13 kΩ) in QAHE. However, an interesting feature is found, bumps indicated by open arrows on the curve in (d). The bumps mean stronger magnetic field than the applied field; it is additional magnetic field originates from the skyrmions. During the reversal of magnetization by the reversal of applied magnetic field, as schematically shown in Fig. 16, skyrmions are formed and produce emergent field due to DMI in the broken SIS situation. The skyrmions are created and stabilized by the chiral

nature in the surface state of massive Dirac cones; without such a chiral electronic state, the magnetization reversal occurs without spiral structures in spin arrangement. The bumps in the Hall resistance at magnetization reversal are a feature of so-called "topological Hall effect", evidence of skyrmion formation. Because of their small size and stability, magnetic skyrmions are expected to be information carriers in spintronics devices [89,90].

9. Concluding Remarks

While , as described in Section 3, electrical conduction through surface states was first confirmed in a trivial and spin-degenerate metallic surface state, such surface-state transport is now very common and important for Rashba and topological insulators due to the spin-related transport phenomena. As introduced here, strong spin-orbit interaction (SOI) and resulting band inversion, Berry curvature and Berry phase, spin-momentum locking, spin-split bands, etc. are novel ingredients for quantum transport phenomena such as spin-polarized current, pure spin current, non-reciprocal photocurrent, topological Hall effect, and so on. Surface-state superconductivity in Rashba-type and topological surface states is especially interesting because it can exhibit unconventional superconductivity beyond the framework of BCS theory, leading to possible spin-polarized supercurrent and Majorana particles at boundaries. These are now hot topics in superconducting spintronics and quantum information technology. Boundaries of quantum materials introduced here are main platforms for such emerging technologies.

Of course, however, there remain lots of fundamental challenges for practical applications of quantum materials and their boundary electronic states. We do not know how to detect pure spin current directly; we do not have a "spin current meter" and a versatile "spin current battery". We need to use some conversion processes between spin current and electrical current, such as the spin Hall effect, Edelstein effect, and so on, but their conversion efficiencies are not generally high. Although some ideas are proposed to use dissipation-less edge current for energy-saving devices, we do not yet have methods for its versatile control. While structural controls of quantum materials are now very advanced on the atomic scale, e.g., with van der Waals epitaxy and stacking control of 2D atomic layers, the detections and controls of physical phenomena such as transport in/on the materials are required to be further develop for future technologies. Another challenge is to discover the quantum

materials and quantum structures compatible with the current microelectronics and semiconductor technology, for which surface and interface physics plays an important role.

Acknowledgments

The results shown here have been achieved through the generous long-term support from JSPS KAKENHI Grants. The most recent grants, numbered 23H00265 and 20H00342, have been particularly instrumental. I am deeply grateful for the contributions of numerous past and present students and research associates in my group, and also external collaborators, whose efforts have been indispensable to these results. Additionally, I would like to acknowledge the valuable discussions held at various meetings and conferences, including those at the long-term Cooperative Research Project of RIEC, Tohoku University, where insights from many experts have greatly aided our research efforts.

References

1) For a review, e.g., S. Hasegawa, X. Tong, S. Takeda, N. Sato, and T. Nagao, Prog. Surf. Sci. **60**, 89 (1999).
2) I. E. Tamm, Phys. Z. Sowjetunion **1**, 733 (1932).
3) I. E. Tamm, Z. Phys. **76**, 849 (1932).
4) W. Shockley, Phys. Rev. **56**, 317 (1939).
5) Y. Ando, J. Phys. Soc. Jpn. **82**, 102001 (2013).
6) M. Z. Hasan and J. E. Moore, Annu. Rev. Condens. Matter Phys.2, 55 (2011).
7) A. K. Geim and K. S. Novoselov, Nature Materials **6**, 183 (2007).
8) A. H. Castro Neto, F. Guinea, N. M. R. Peres, K. S. Novoselov, and A. K. Geim, Rev. Mod. Phys. **81**, 109 (2009).
9) K. S. Novoselov, A. K. Geim, S. V. Morozov, D. Jiang, M. I. Katsnelson, I. V. Grigorieva, S. V. Dubonos, and A. A. Firsov, Nature **438**, 197 (2005).
10) Y. Zhang, Y.-W. Tan, H. L. Stormer, and P. Kim, Nature **438**, 201 (2005).
11) M. König, S. Wiedmann, C. Brüne, A. Roth, H. Buhmann, L. W. Molenkamp, X.-L. Qi, S.-C. Zhang, Science **318**, 766 (2007).
12) B. A. Bernevig, T. L. Hughes, S.-C. Zhang, Science **314**, 1757 (2006).
13) Y. Ren, Z. Qiao and Q. Niu, Rep. Prog. Phys. **79**, 066501 (2016).

14) F. Liu, Coshare Science 01, video-3, 1-62 (2023) (DOI: https://doi.org/10.61109/cs.202310.115)
15) M. Sato and Y. Ando, Rep. Prog. Phys. **80**, 076501 (2017).
16) G. C. Ménard, S. Guissart, C. Brun, R. T. Leriche, M. Trif, F. Debontridder, D. Demaille, D. Roditchev, P. Simon, and T. Cren, Nat. Comm. **8**, 2040 (2017).
17) C. Oshima and A. Nagashima, J. Phys.: Condens. Matter **9**, 1 (1997).
18) P. Vogt, P. De Padova, C. Quaresima, J. Avila, E. Frantzeskakis, M. C. Asensio, A. Resta, B. Ealet, and G. Le Layr, Phys. Rev. Lett. **108**, 155501 (2012).
19) M. E. Dávila, L. Xian, S. Cahangirov, A. Rubio, and G. Le Lay, New J. Phys. **16**, 095002 (2014).
20) F.-f. Zhu, W.-j. Chen, Y. Xu, C.-l. Gao, D.-d. Guan, C.-h. Liu, D. Qian, S.-C. Zhang, and J.-f. Jia, Nature Materials **14**, 1020 (2015).
21) J. Yuhara, B. He, N. Matsunami, M. Nakatake, and G. Le Lay, Advanced Materials **31**, 1901017 (2019).
22) For a review, S. Hasegawa, N. Sato, I. Shiraki, C. L. Petersen, P. Boggild, T. M. Hansen, T. Nagao, F. Grey, Japanese Journal of Applied Physics **39**, 3815 (2000)
23) T. Takahashi, K. Sugawara, S. Ichinokura, A. Takayama, and S. Hasegawa, Hyomen Kagaku **38**, 460 (2017). [in Japanese, but figures and their captions in English]
24) G. Nicolay, F. Reinert, S. Hüfner, and P. Blaha, Phys. Rev. B **65**, 033407 (2001)
25) D. V. Gruznev, L. V. Bondarenko, A. V. Matetskiy, A. A. Yakovlev, A. Y. Tupchaya, S. V. Eremeev, E. V. Chulkov, J.-P. Chou, C.-M. Wei, M.-Y. Lai, Y.-L. Wang, A. V. Zotov, and A. A. Saranin, Scientific Reports **4**, 4742 (2014).
26) A.V. Matetskiy, S. Ichinokura, L.V. Bondarenko, A.Y. Tupchaya, D.V. Gruznev, A.V. Zotov, A.A. Saranin, R. Hobara, A. Takayama, and S. Hasegawa, Phys. Rev. Lett. **115**, 147003 (2015)
27) H. Zhang, C.-X. Liu, X.-L. Qi, X. Dai, Z. Fang, and S.-C. Zhang, Nature Phys. **5**, 438 (2009).
28) M. Z. Hasan and C. L. Kane, Rev. Mod. Phys. **82**, 3045 (2010).
29) T. Hirahara, S. V. Eremeev, T. Shirasawa, Y. Okuyama, T. Kubo, R. Nakanishi, R. Akiyama, A. Takayama, T. Hajiri, S. Ideta, M. Matsunami, K. Sumida, K. Miyamoto, Y. Takagi, K. Tanaka, T. Okuda, T.Yokoyama, S. Kimura, S. Hasegawa, and E. V. Chulkov,

Nano Letters **17**, 3493 (2017).

30) J. Li, Y. Li, S. Du, Z. Wang, B.-L. Gu, S.-C. Zhang, K. He, W. Duan, Y. Xu, Science Adv. **5**, eaaw5685 (2019).
31) Y. Deng, Y. Yu, M. Z. Shi, Z. Guo, Z. Xu, J. Wang, X. H. Chen, Y. Zhang, Science **367**, 895 (2020).
32) T. Takahashi, S. Nakatani, N. Okamoto, T. Ishikawa, and S. Kikuta, Jpn. J. Appl. Phys. **27**, L753 (1988).
33) J. H. Lee, G. W. Kim, I. Song, Y. Kim, Y. Lee, S. J. Yoo,D.-Y. Cho, J.-W. Rhim, J. Jung, G. Kim, and C. Kim, arXiv:2401.00265 (2024).
34) T. Hirahara, I. Matsuda, M. Ueno, and S. Hasegawa, Surface Science **563**, 191 (2004).
35) T. Hirahara, I. Matsuda, and S. Hasegawa, e-Journal of Surface Science and Nanotechnology **2**, 141 (2004)
36) H. Aizawa, M. Tsukada, N. Sato, and S. Hasegawa, Surface Science **429**, L509 (1999).
37) C. Liu, I. Matsuda, R. Hobara, and S. Hasegawa, Phys. Rev. Lett. **96**, 036803 (2006) .
38) N. Sato, T. Nagao, and S. Hasegawa, Physical Review B **60**, 16083 (1999).
39) Y. Nakajima, S. Takeda, T. Nagao, S. Hasegawa, and X. Tong, Physical Review B **56**, 6782 (1997).
40) W. Norimatsu and M. Kusunoki, Chem. Phys. Lett. **468**, 52 (2009).
41) K. S. Novoselov, Z. Jiang, Y. Zhang, S. V. Morozov, H. L. Stormer, U. Zeitler, J. C. Maan, G. S. Boebinger, P. Kim, and A. K. Geim, Science **315**, 1379 (2007).
42) S. Ichinokura, K. Sugawara, A. Takayama, T. Takahashi, and S. Hasegawa, ACS Nano **10**, 2761 (2016).
43) Y. Xu, X. Li, and J. Dong, Nanotechnology **21**, 065711 (2010).
44) R. Akiyama, Y. Takano, Y. Endo, S. Ichinokura, R. Nakanishi, K. Nomura, and S. Hasegawa, Appl. Phys. Lett. **110**, 233106 (2017).
45) Y. Cao, V. Fatemi, A. Demir, S. Fang, S. L. Tomarken, J. Y. Luo, J. D. Sanchez-Yamagishi, K. Watanabe, T. Taniguchi, E. Kaxiras, R. C. Ashoori, and P. Jarillo-Herrero, Nature **556**, 80 (2018).
46) J. B. Goodenough and K.-S. Park, JACS **135**, 11267 (2013).
47) H. Toyama, R. Akiyama, M. Hashizume, S. Ichinokura, T. Iimori, T. Matsui, K. Horii, S.

Sato, R. Hobara, Y. Endo, T. Hirahara, F. Komori, S. Hasegawa, ACS Nano **16**, 3582 (2022).

48) Y. Endo, Y. Fukaya, I. Mochizuki, A. Takayama, T. Hyodo, S. Hasegawa, Carbon **157**, 857 (2020).
49) Y. Endo, M. Li, R. Akiyama, X. Yan, C. Brandl, J. Z. Liu, R. Hobara, S. Hasegawa, W. Wan, K. S. Novoselov and W.-X. Tang, Nature Nanotechnology **18**, 1154 (2023).
50) Y. Cao, V. Fatemi, S. Fang, K. Watanabe, T. Taniguchi, E. Kaxiras, and P. Jarillo-Herrero, Nature **556**, 43 (2018)
51) E. I. Rashba, Sov. Phys. Sol. St. **2**, 1109 (1960).
52) Y. A. Bychkov and E. I. Rashba: J. Phys., C **17**, 6039 (1984).
53) M. Nagano, A. Kodama, T. Shishidou and T. Oguchi: J. Phys. Condens. Matter, **21**, 064239 (2009).
54) For a review, J. H. Dill, J. Phys.: Condens. Matter **21**, 403001 (2009).
55) C. Bigi, P. K. Das, D. Benedetti, F. Salvador, D. Krizmancic, R. Sergo, A. Martin, G. Panaccione, G. Rossi, J. Fujii, and I. Vobornik, J. Synchrotron Radiation **24**, 750 ((2017).
56) M. Yamada, T. Hirahara, S. Hasegawa, H. Mizuno, Y. Miyatake, and T. Nagamura, e-J. Surf. Sci. Nanotechnol. **10**, 400 (2012).
57) S. Hasegawa, J. Phys.: Cond. Matt. **31**, 223001 (2019).
58) P. Fulde and R. A. Ferrell, Phys. Rev. **135** (3A), A550 (1964).
59) A. I. Larkin and Y. N. Ovchinnikov, Sov. Phys. JETP. **20**, 762 (1965).
60) L. P. Gor'kov and E. I. Rashba, Phys. Rev. Lett. **87**, 037004 (2001).
61) J. Linder and J. W. A. Robinson, Nat. Phys. **11**, 307 (2015).
62) T. Nakamura, H. Kim, S. Ichinokura, A. Takayama, A.V. Zotov, A.A. Saranin, Y. Hasegawa, and S. Hasegawa, Phys. Rev. B **98**, 134505 (2018).
63) T. Machida, Y. Yoshimura, T. Nakamura, Y. Kohsaka, T. Hanaguri, C.-R. Hsing, C.-M. Wei, Y. Hasegawa, S. Hasegawa, and A. Takayama, Phys. Rev. B **105**, 064507 (2022).
64) Y. Aharonov and D. Bohm, Phys. Rev. 115, 485(1959).
65) S. Borisova, J. Krumrain, M. Luysberg, G. Mussler, and D. Grützmacher, Cryst. Growth Des. **12**, 6098 (2012).
66) A. Koma, Thin Solid Films 216, 72 (1992).
67) Y. Sakamoto, T. Hirahara, H. Miyazaki, S. Kimura, and S. Hasegawa, Phys. Rev. B **81**,

165432 (2010).

68) T. Hirahara, Y. Sakamoto, Y. Takeichi, H. Miyazaki, S. Kimura, I. Matsuda, A. Kakizaki, and S. Hasegawa, Phys. Rev. B **82**, 155309 (2010).

69) Y. Xia, D. Qian, D. Hsieh, L. Wray, A. Pal, H. Lin, A. Bansil, D. Grauer, Y. S. Hor, R. J. Cava, and M. Z. Hasan, Nat. Phys. **5**, 398 (2009).

70) W. Zhang, R. Yu, H.-J. Zhang, X. Dai and Z. Fang, New J. Phys. **12**, 065013 (2010).

71) M. Aitani, Y. Sakamoto, T. Hirahara, M. Yamada, H. Miyazaki, M. Matsunami, S. Kimura, and S. Hasegawa, Japanese Journal of Applied Physics **52**, 110112 (2013).

72) By Yao-Yi Li , Guang Wang , Xie-Gang Zhu , Min-Hao Liu , Cun Ye , Xi Chen , Ya-Yu Wang , Ke He , Li-Li Wang , Xu-Cun Ma , Hai-Jun Zhang , Xi Dai , Zhong Fang , Xin-Cheng Xie, Ying Liu , Xiao-Liang Qi , Jin-Feng Jia , * Shou-Cheng Zhang , and Qi-Kun Xue, Advanced Materials 22, 4002 (2010).

73) S. Hasegawa, I. Shiraki, F. Tanabe, R. Hobara, T. Kanagawa, T. Tanikawa, I. Matsuda, C. L. Petersen, T. M. Hansen, P. Boggild, and F. Grey, Surface Review and Letters 10, 963 (2003).

74) L. Barreto, L. Kühnemund, F. Edler, C. Tegenkamp, J. Mi, M. Bremholm, B. B. Iversen, C. Frydendahl, M. Bianchi, and P. Hofmann, Nano Lett. **14**, 3755 (2014).

75) K. Hoefer, C. Becker, D. Rata, and L. H. Tjeng, Proc. Natl. Acad. Sci. U.S.A. **111**, 14979 (2014)

76) M. König, S. Wiedmann, C. Brüne, A. Roth, H. Buhmann, L. W. Molenkamp, X.-L. Qi, S. -C. Zhang, Science **318**, 766 (2007).

77) Liu; B. Huang, K-H Jin, B. Cui, F. Zhai, J. Mei and Feng Liu. Nature Comm. **8**, 15850 (2017).

78) J. W. McIver, D. Hsieh, H. Steinberg, P. Jarillo-Herrero, and N. Gedik, Nature Nanotechnology **7**, 96 (2012).

79) D. Fan, R. Hobara, R. Akiyama, and S. Hasegawa, Phys. Rev. Research **2**, 023055 (2020).

80) I. Taniuchi, R. Akiyama, R. Hobara, and S. Hasegawa, arXiv:2308.02485 (2023).

81) C.-Z. Chang, J. Zhang, X. Feng, J. Shen, Z. Zhang, M. Guo, K. Li, Y. Ou, P. Wei, L.-L. Wang, Z.-Q. Ji, Y. Feng, S. Ji, X. Chen, J. Jia, X. Dai, Z. Fang, S.-C. Zhang, K. He, Y. Wang, L. Lu, X.-C. Ma, Q.-K. Xue, Science **340**, 167 (2013).

82) M. Mogi, R. Yoshimi, A. Tsukazaki, K. Yasuda, Y. Kozuka, K. S. Takahashi, M. Kawasaki, and Y. Tokura, Appl. Phys. Lett. **107**, 182401 (2015).

83) Y. Deng, Y. Yu, M. Z. Shi, Z. Guo, Z. Xu, J. Wang, X. H. Chen, Y. Zhang, Science **367**, 895

(2020).
84) For a review, Y. Tokura and N. Kanazawa, Chemical Review **121** (5), 2857 (2021).
85) I. Dzyaloshinskii, Journal of Physics and Chemistry of Solids **4** (4), 241 (1958).
86) T. Moriya, Physical Review **120** (1), 91 (1960).
87) T. Takashiro, R. Akiyama, I. A. Kibirev, A. V. Matetskiy, R. Nakanishi, S. Sato, T. Fukasawa, T. Sasaki, H. Toyama, K. L. Hiwatari, A. V. Zotov, A. A. Saranin, T. Hirahara, S. Hasegawa, Nano Letters **22** (3), 881 (2022).
88) S. Hasegawa, "Reflection high-energy electron diffraction", pp. 1925-1938, in *Characterization of Materials*, ed. E. N. Kaufmann. (John Wiley & Sons, 2012).
89) C. H. Marrows and K. Zeissier, Appl. Phys. Lett. **119**, 250502 (2021).
90) A. Fert and F. N. Van Dau, Comptes Rendus Physique **20**, 817 (2019).

Figure Captions

Fig. 1. Surface electronic states originated from various mechanisms. (a) Spill out of electron wave on a metal surface. (b) Dangling bonds on a semiconductor surface. (c) Formation of "surface alloys" on a substrate. (d) Topological surface states on a topological insulator.

Fig. 2. Various types of band dispersions of surface states. (a) A spin-degenerate parabolic dispersion. (b) A spin-degenerate linear dispersion (so-called "Dirac cone"). (c) Rashba-type spin-split surface states. (d) A helical Dirac cone of a topological insulator. (e) A chiral Dirac cone with an edge state on a magnetic topological insulator.

Fig. 3. Si(111)-$\sqrt{3} \times \sqrt{3}$-Ag surface superstructure. (a) The atomic arrangement. Filled (open) circles are Ag (Si) atoms [21]. (b)-(d) The surface-state band observed at room temperature (RT) by angle-resolved photoemission spectroscopy, with additional adsorption of tiny amounts of Au adatoms, 0.01 ML (b), 0.02 ML (c), and 0.03 ML (d), respectively [36]. (e) A scanning tunneling microscopy image at 6 K, showing additional Ag atoms on Si(111)-$\sqrt{3} \times \sqrt{3}$-Ag surface [37]. (f) Electrical resistance drops measured at RT, caused by tiny amounts of additional Ag adsorption [1,38].

Fig. 4. Graphene and intercalation therein. (a)-(c) Cross-sectional transmission electron

microscopy images of monolayer graphene (a), bi-layer graphene (b), and tri-layer graphene (c) grown on SiC(0001) crystal substrate, respectively [39]. (d)(e) Band dispersions of monolayer graphene (d), and by-layer graphene (e) [22], respectively. (f)(g) Side-view schematics of monolayer graphene grown on SiC(0001) (f), and after Li/Ca atoms-intercalation (g). (h) Electrical resistance changes of pristine monolayer graphene, and after Li/Ca intercalation as a function of temperature [41,46].

Fig. 5. A schematic showing the influence on the momentum and spin of an electron caused by time-reversal operation (a) and space-inversion operation (b).

Fig. 6. The situation of surface-state electrons. (a) Change of electron energy near the crystal surface. The potential for an electron is lower inside the material due to the work function which is equal to the difference between the vacuum level and the Fermi level. (b) A side-view schematic near a crystal surface. (c) A parallel-plate capacitor, mimicking the electric field due to the work function at the crystal surface. (d) An electron moving in the capacitor, mimicking the surface-state electron moving along the crystal surface, in the view of laboratory system. (e) The same situation in the view of rest frame of the electron. (f) Virtual (emergent) magnetic field felt by the electron in its rest frame.

Fig. 7. The Rashba effect on surface-state electrons. The band splitting viewed in (a) the band dispersion and (b) Fermi surface. Short arrows indicate the direction of spin of each electron. (c) The surface-state band of Au(111) crystal, measured by spin- and angle-resolved photoemission spectroscopy (SARPES) [54]. (d) A schematic illustrating the motion and spin of surface-state electrons on Au(111).

Fig. 8. Si(111)-$\sqrt{3} \times \sqrt{3}$-(Tl,Pb) surface superstructure. (a) Its atomic arrangement [24], (b) STM image [25], and (c) RHEED patten. (d) Its band dispersion measured by ARPES and (e) that calculated by density-functional theory [24,25]. (f) Its sheet resistance as a function of temperature, showing superconductivity [25].

Fig. 9. Scanning tunneling spectroscopy measurements of Si(111)-$\sqrt{3} \times \sqrt{3}$-(Tl,Pb) surface superstructure at 0.5 K. (a)-(d) Zero-bias conductance maps under surface-normal magnetic field of 0 T (a), 0.1 T (b), 0.2 T (c), and 1.2 T (d), respectively [61]. The scan area is 1 μm × 1 μm. (e) STS spectra measured at a point outside of a vortex (red curves) and at the center of a vortex (black curves) under different magnetic fields.

Fig. 10. Topological insulators. (a) A schematic of bands of a trivial insulator/semiconductor, (b) band crossing/inversion due to energy shift by spin-orbit interaction, and (c) re-opening of a band gap (a non-trivial band gap) in the interior of a topological insulator. (d)(e) Schematics showing the phase of band electrons in the trivial (d) and non-trivial (e) insulators, respectively. (f) A schematic of the band dispersion in the momentum space, showing the topological surface-state bands spanning the non-trivial band gap between the bulk conduction and valence bands.

Fig. 11. (a) The atomic-layer stacking structure in typical topological insulators, Bi_2Se_3 and Bi_2Te_3. (b) Cross-sectional transmission electron microscopy (XTEM) image of Bi_2Te_3(111) thin film epitaxially grown on Si(111) substrate [64]. (c)(d) ARPES band dispersion images of a 3 QL-thick (c) and 8 QL-thick (d) Bi_2Te_3(111) thin films grown on Si(111), respectively [66].

Fig. 12. Three QL-thick Bi_2Te_3 thin films grown on Si(111) substrate with Pb-atom doping [70]. (a)-(f) Fermi surface (upper row) and band dispersion (lower row) near the Fermi level with the Pb concentration of 0 (a), 1.3 (b), 3.2 (c), 8.7 (d), 14 (e), and 22% (f), respectively. The line in the band dispersion diagrams indicates the position of the Dirac point. B and S represent the bulk and surface states, respectively. (g) Change of the carrier densities in the bulk and surface states of the Bi_2Te_3 thin films as a function of Pb concentration, calculated from area of the measured Fermi surfaces (a)-(f). (h) The change in the Dirac point position (from (a)-(f)) (red data points), together with the measured 2D sheet conductivity (blue data points) as a function of Pb concentration.

Fig. 13. (a) The surface-sate band of a topological insulator, showing spin of each electron, forming a so-called helical Dirac cone. (b) An energy contour in the Dirac cone, showing the spin-momentum locking. (c)(d) Motions of surface-state electrons on three- (c) and two-dimensional (d) topological insulators in real space.

Fig. 14. (a) Spin-selective optical excitations in topological surface states, resulting in production of one-way (non-reciprocal) photocurrent flowing. (b) A Fermi-surface shift due to injection of in-plane spin s_x, producing electrical current in y direction (the inverse Rashba-Edelstein effect). (c) An experimental set-up to measure the photo-current depending on the polarization of light shining on a topological insulator in ultrahigh vacuum (UHV).

(d) Change in photocurrent measured on Bi_2Se_3 thin film (13 QL thick) grown on Si(111) depending on the polarization of the shining light (the wavelength of light $\lambda = 1550$ nm, and the angle of incidence of light $\theta = 40^{\circ}$) [77].

Fig. 15. Atomic-layer stacking structures, ARPES band dispersion images, and schematic illustrations of the surface states of Bi_2Se_3 (a) and $MnBi_2Se_4/Bi_2Se_3$ heterostructure, respectively [28]. A derivative image of ARPES band dispersion is also shown in (b).

Fig. 16. A topological-insulator layer sandwiched between layers of a ferromagnetic topological insulator [85]. (a) A schematic of the sandwich heterostructure ($Mn(Bi,Sb)_2Te_4/(Bi,Sb)_2Te_4/Mn(Bi,Sb)_2Te_4$) grown on Si(111) substrate. (b) Its STEM image, and (c) RHEED pattern taken after the growth. (d) Its Hall resistance (after subtracting the component of ordinary Hall effect) measured at 0.5 K as a function of magnetic field applied in the surface-normal direction, and schematics of magnetization during the field sweeping.

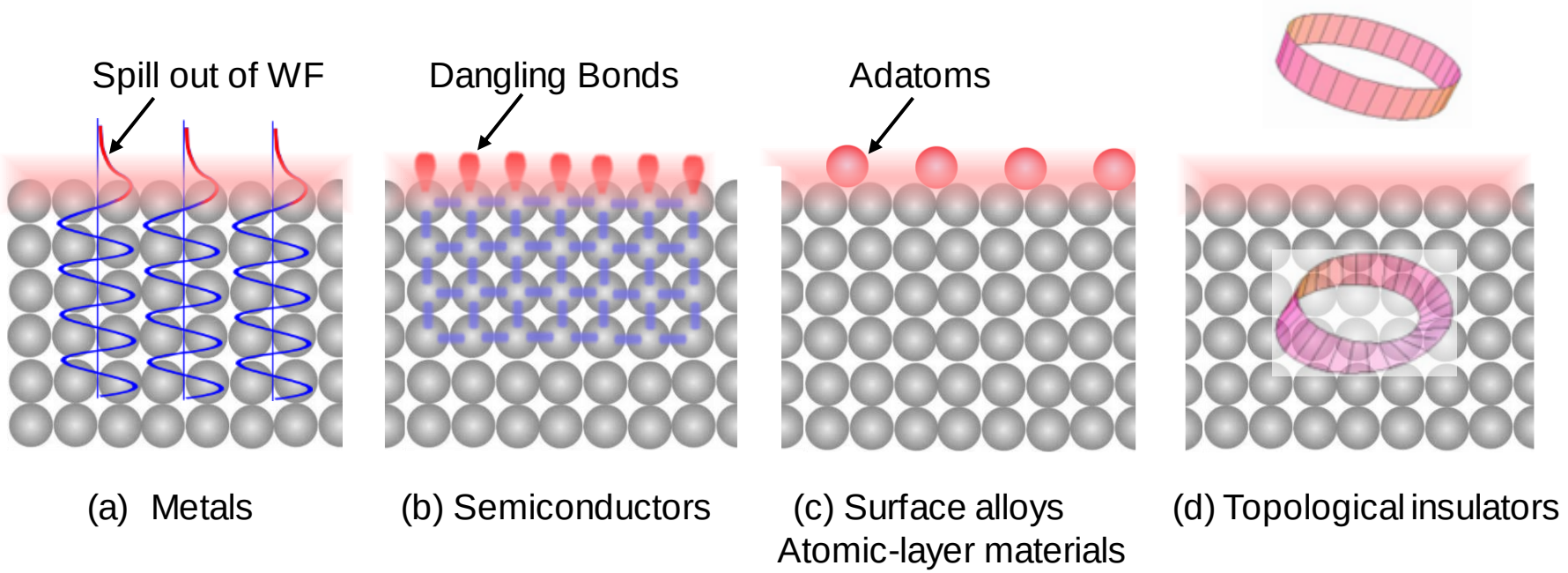
Spill out of WF
Dangling Bonds
Adatoms
(a) Metals
(b) Semiconductors
(c) Surface alloys
Atomic-layer materials
(d) Topological insulators

Fig. 1

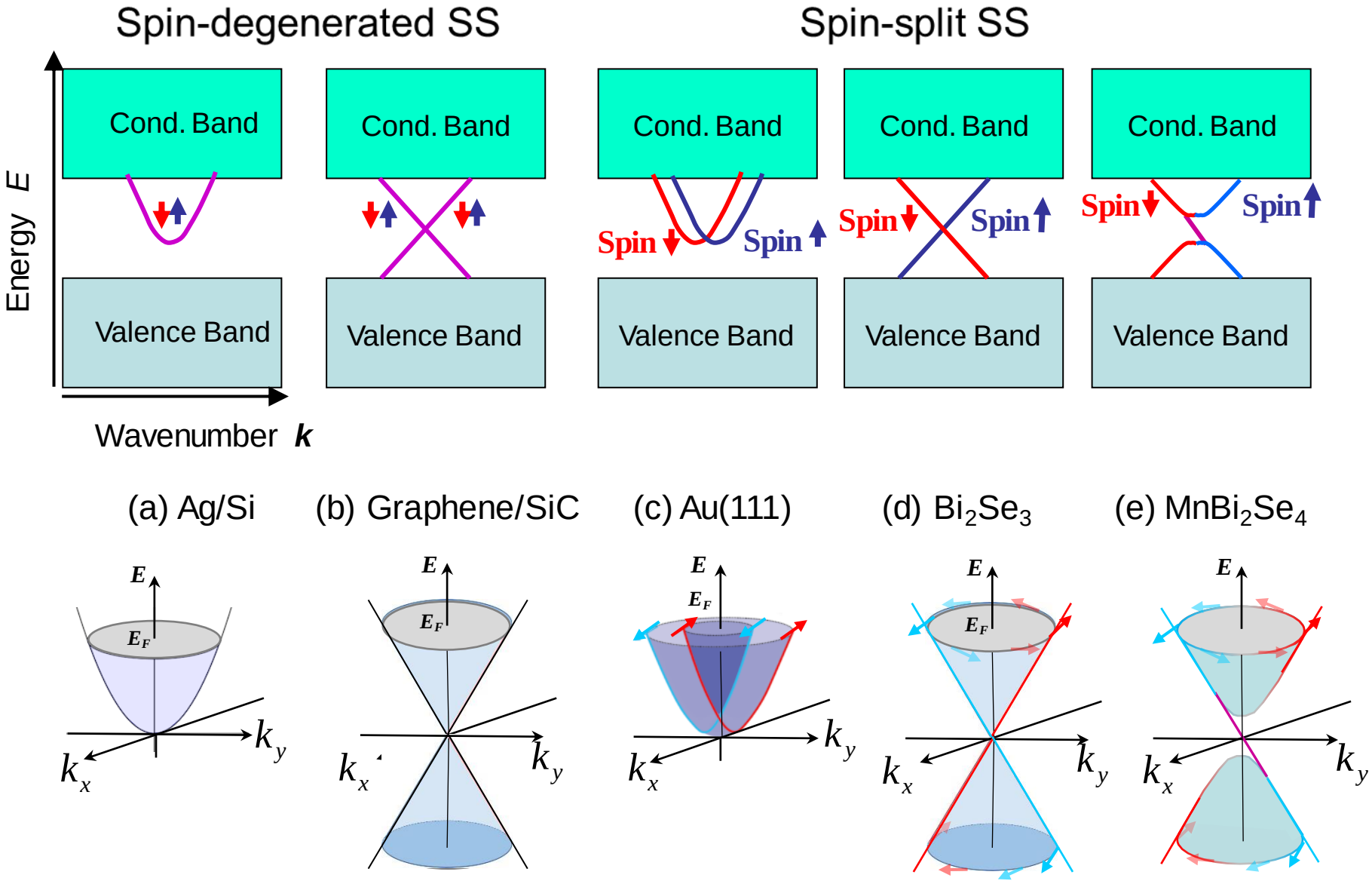
Spin-degenerated SS
Spin-split SS
Energy E
Cond. Band
Valence Band
Wavenumber k
Spin
(a) Ag/Si
(b) Graphene/SiC
(c) Au(111)
(d) Bi2Se3
(e) MnBi2Se4
E
EF
kx
ky

Fig. 2

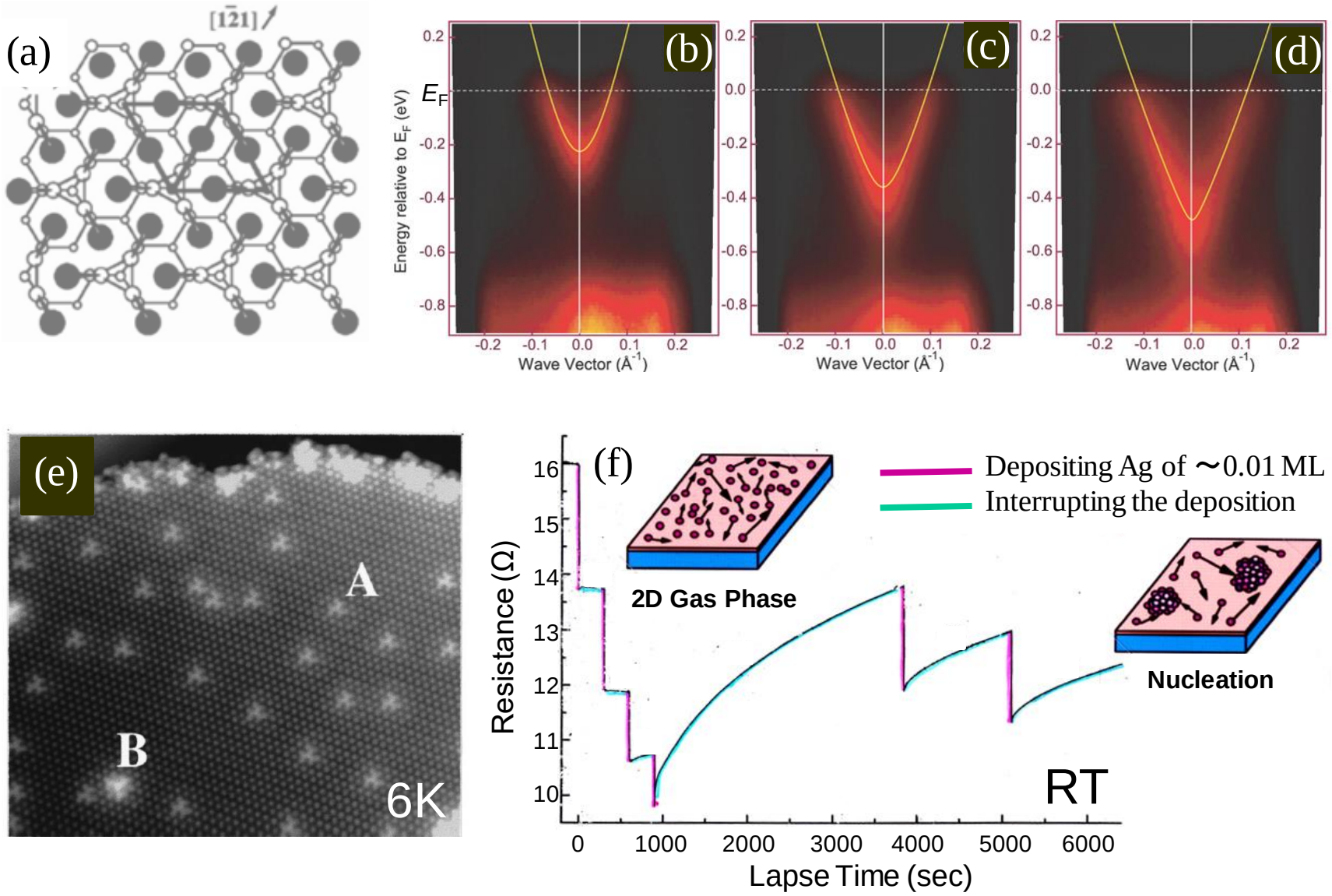
(a)
[1̄21]
(b)
(c)
(d)
E_F
Energy relative to E_F (eV)
Wave Vector (Å^{-1})
(e)
A
B
6K
(f)
Depositing Ag of ~0.01 ML
Interrupting the deposition
2D Gas Phase
Nucleation
Resistance (Ω)
Lapse Time (sec)
RT

Fig. 3

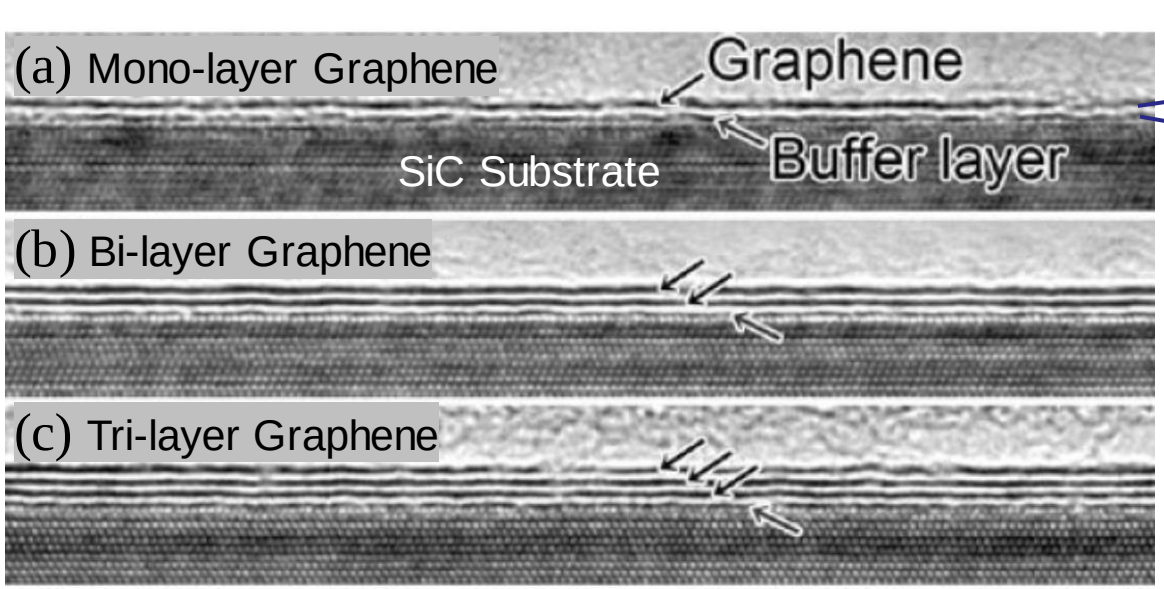
(a) Mono-layer Graphene
Graphene
SiC Substrate
Buffer layer
(b) Bi-layer Graphene
(c) Tri-layer Graphene

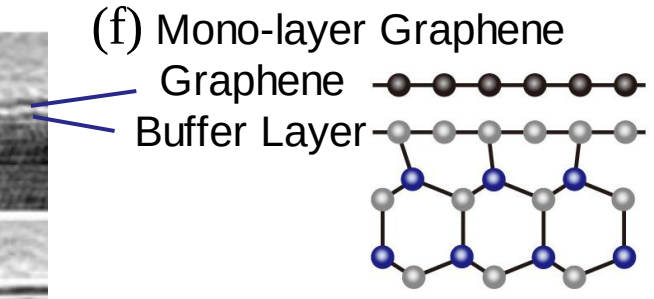
(f) Mono-layer Graphene
Graphene
Buffer Layer

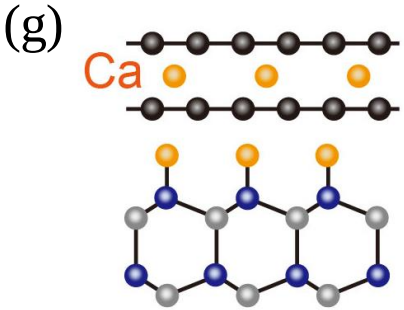
(g)
Ca

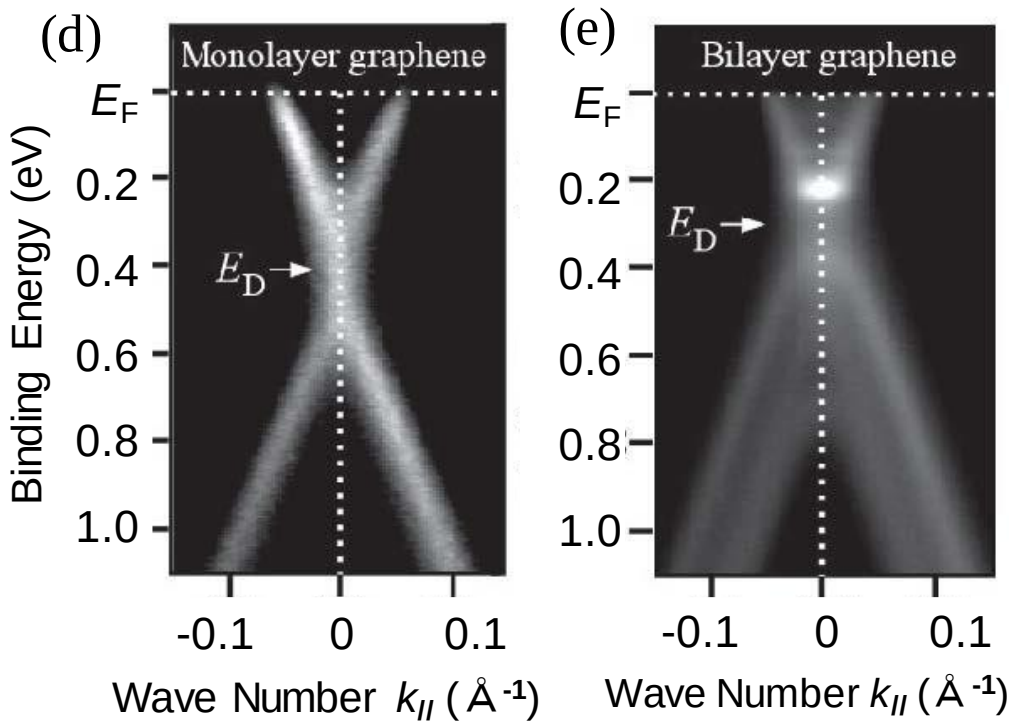
(d)
Monolayer graphene
E_F
0.2
0.4
0.6
0.8
1.0
E_D
Binding Energy (eV)
-0.1
0
0.1
Wave Number $k_{//}$ (Å^{-1})
(e)
Bilayer graphene
E_F
0.2
0.4
0.6
0.8
1.0
F_D
-0.1
0
0.1
Wave Number $k_{//}$ (Å^{-1})

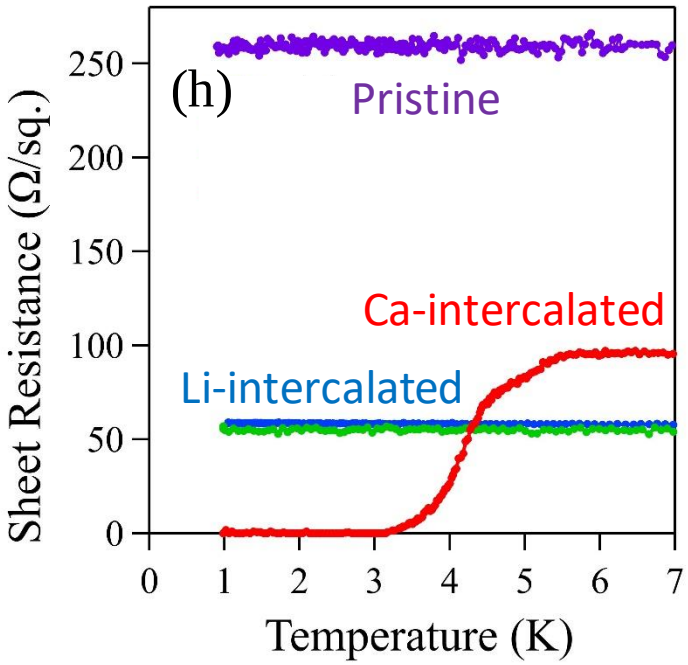
(h)
Pristine
Ca-intercalated
Li-intercalated
Sheet Resistance (Ω/sq.)
250
200
150
100
50
0
0
1
2
3
4
5
6
7
Temperature (K)

Fig. 4

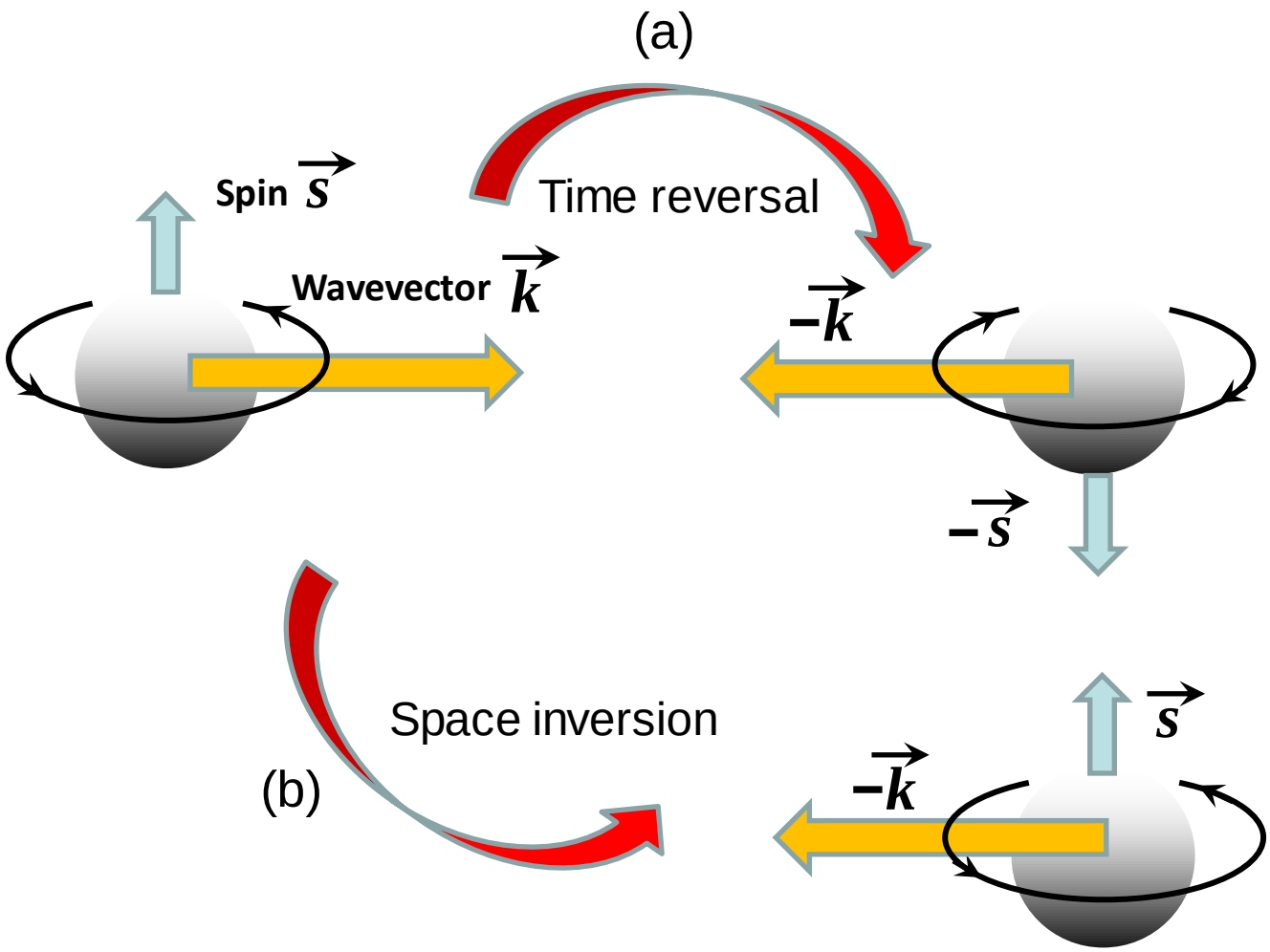
(a)
Spin $\vec{s}$
Time reversal
Wavevector $\vec{k}$
$-\vec{k}$
$-\vec{s}$
Space inversion
(b)
$\vec{s}$
$-\vec{k}$

Fig. 5

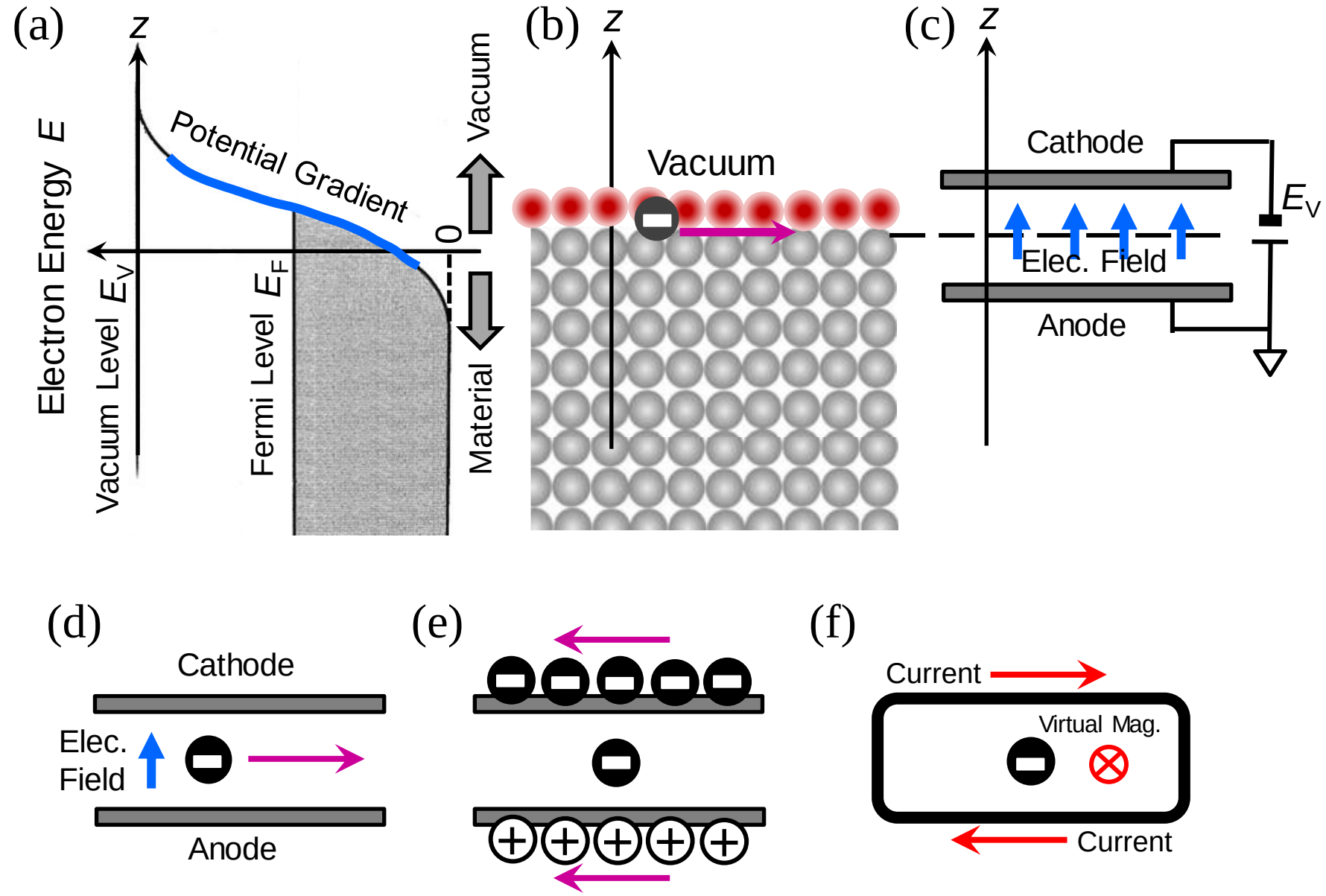
(a)
z
Electron Energy E
Potential Gradient
Vacuum Level E_V
Fermi Level E_F
0
Vacuum
Material
(b)
z
Vacuum
(c)
z
Cathode
E_V
Elec. Field
Anode
(d)
Cathode
Elec.
Field
Anode
(e)
(f)
Current
Virtual Mag.
Current

Fig. 6

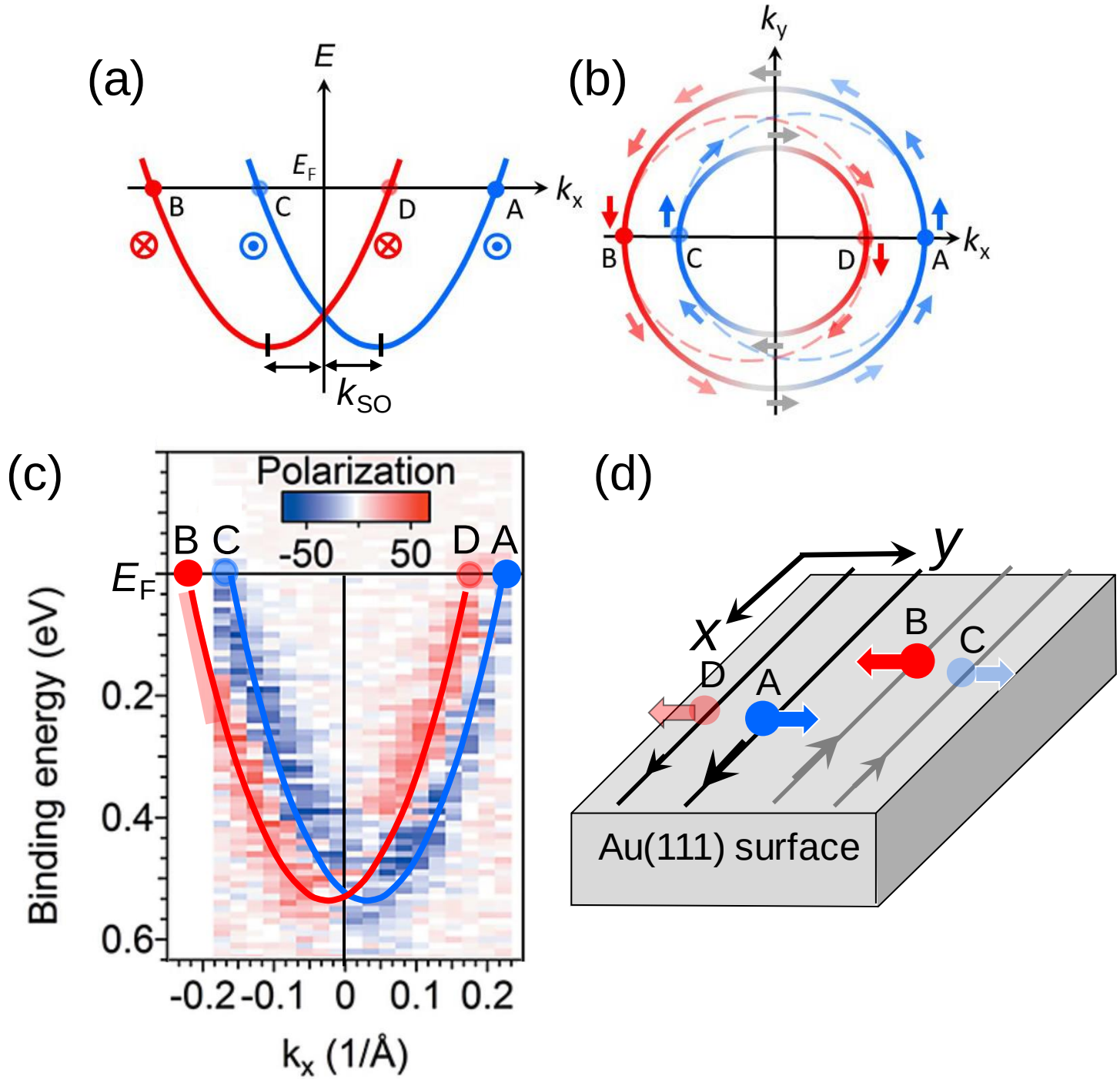
(a)
E
E_F
B
C
D
A
k_x
k_{SO}
(b)
k_y
B
C
D
A
k_x
(c)
Polarization
-50
50
B C
D A
E_F
Binding energy (eV)
0.2
0.4
0.6
-0.2 -0.1 0 0.1 0.2
k_x (1/Å)
(d)
y
x
B
C
D
A
Au(111) surface

Fig. 7

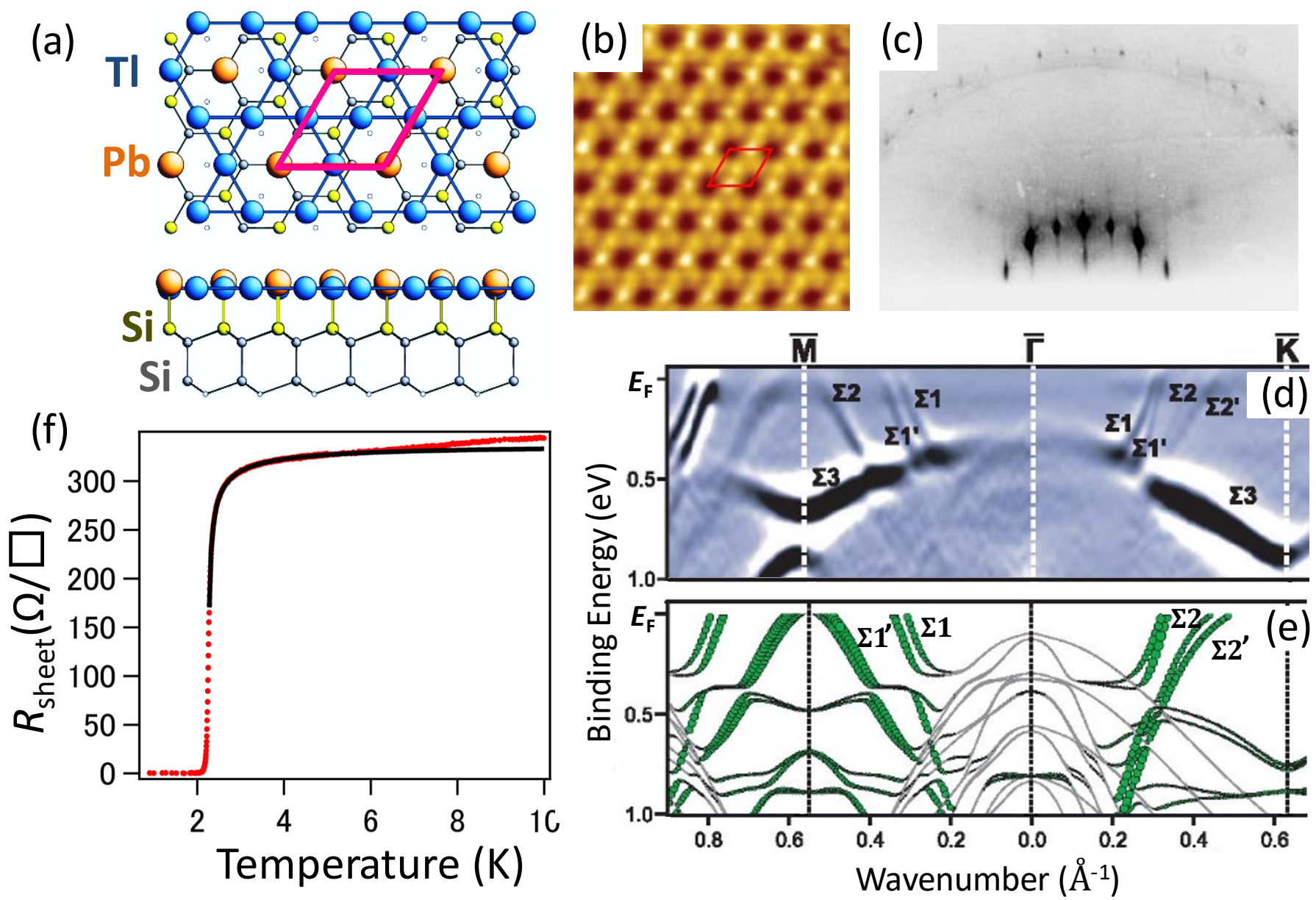
(a)
Tl
Pb
Si
Si
(b)
(c)
(d)
(e)
(f)
M
Γ
K
E_F
Σ2
Σ1
Σ1'
Σ3
Σ2'
Binding Energy (eV)
0.5
1.0
Σ1'
Σ1
Σ2
Σ2'
0.8
0.6
0.4
0.2
0.0
0.2
0.4
0.6
Wavenumber (Å^{-1})
R_{sheet}(Ω/□)
300
250
200
150
100
50
0
2
4
6
8
10
Temperature (K)

Fig. 8

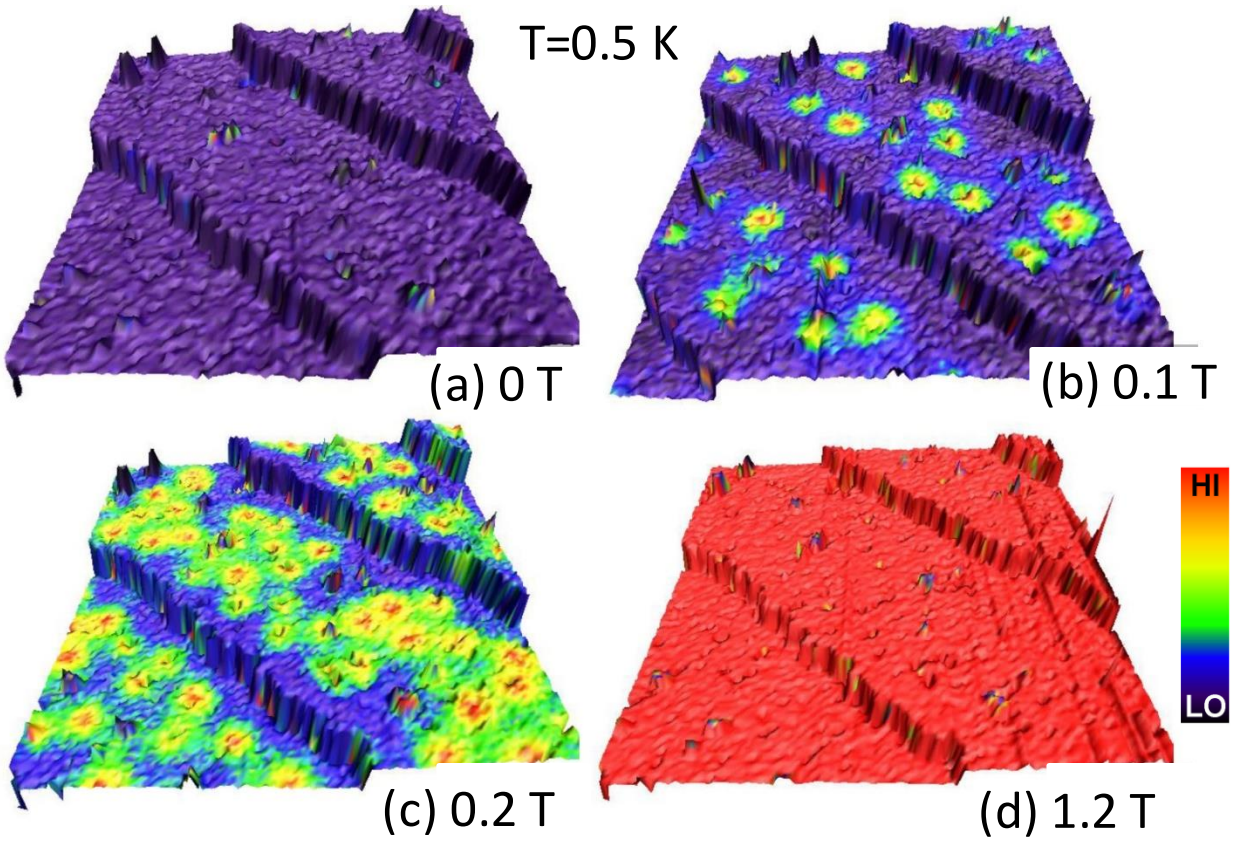
T=0.5 K
(a) 0 T
(b) 0.1 T
(c) 0.2 T
(d) 1.2 T
HI
LO

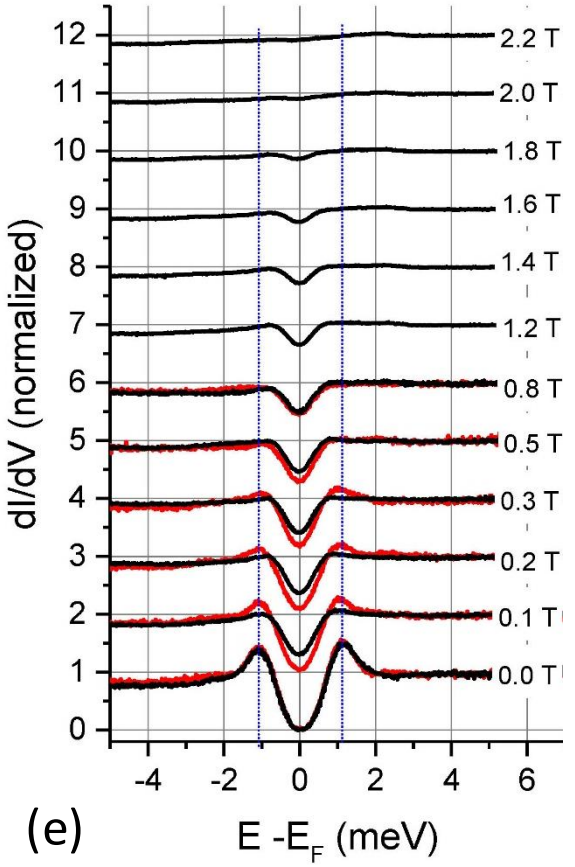
dI/dV (normalized)
E -E$_F$ (meV)
2.2 T
2.0 T
1.8 T
1.6 T
1.4 T
1.2 T
0.8 T
0.5 T
0.3 T
0.2 T
0.1 T
0.0 T
(e)

Fig. 9

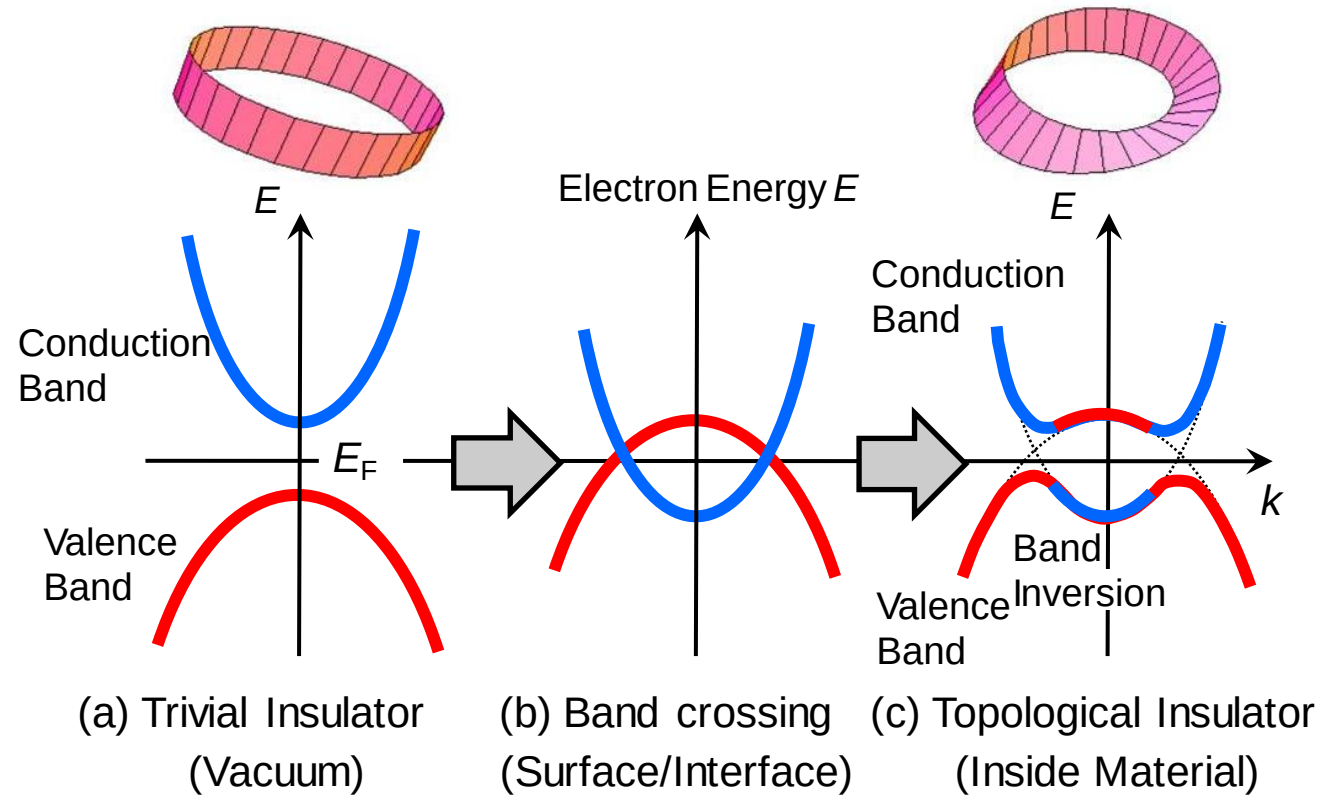
E
Conduction Band
E_F
Valence Band
(a) Trivial Insulator (Vacuum)
Electron Energy E
(b) Band crossing (Surface/Interface)
E
Conduction Band
Band Inversion
Valence Band
k
(c) Topological Insulator (Inside Material)

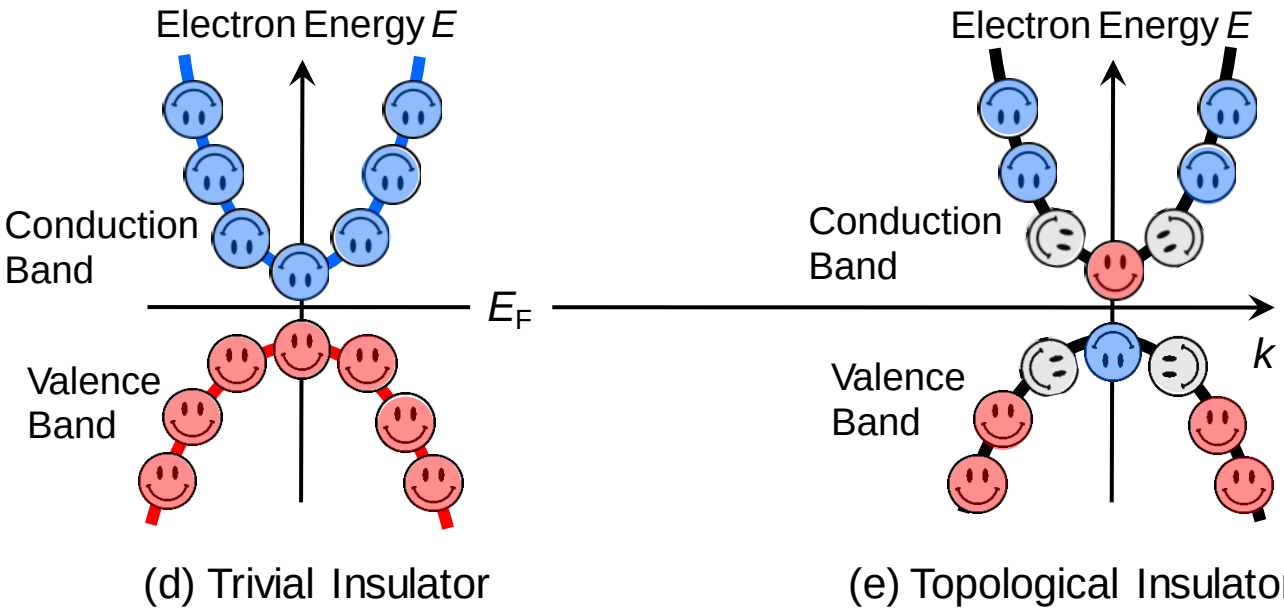
Electron Energy E
Conduction Band
E_F
Valence Band
(d) Trivial Insulator
Electron Energy E
Conduction Band
Valence Band
k
(e) Topological Insulator

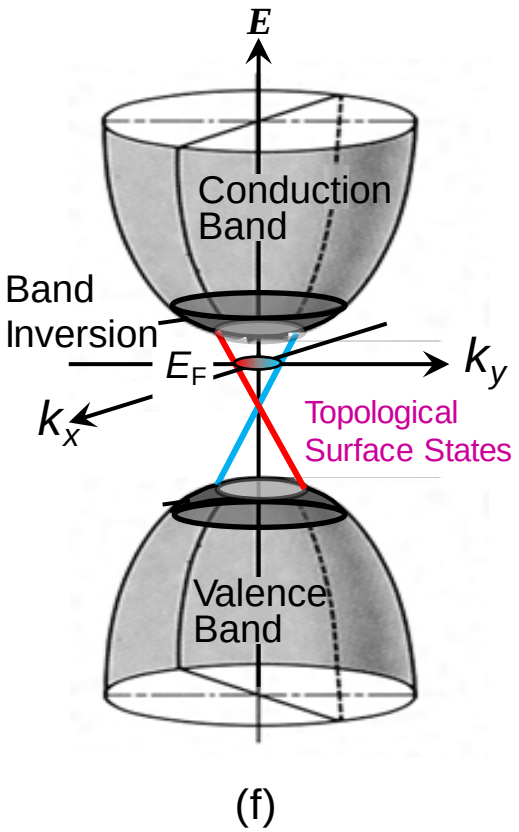
E
Conduction Band
Band Inversion
E_F
k_y
k_x
Topological Surface States
Valence Band
(f)

Fig. 10

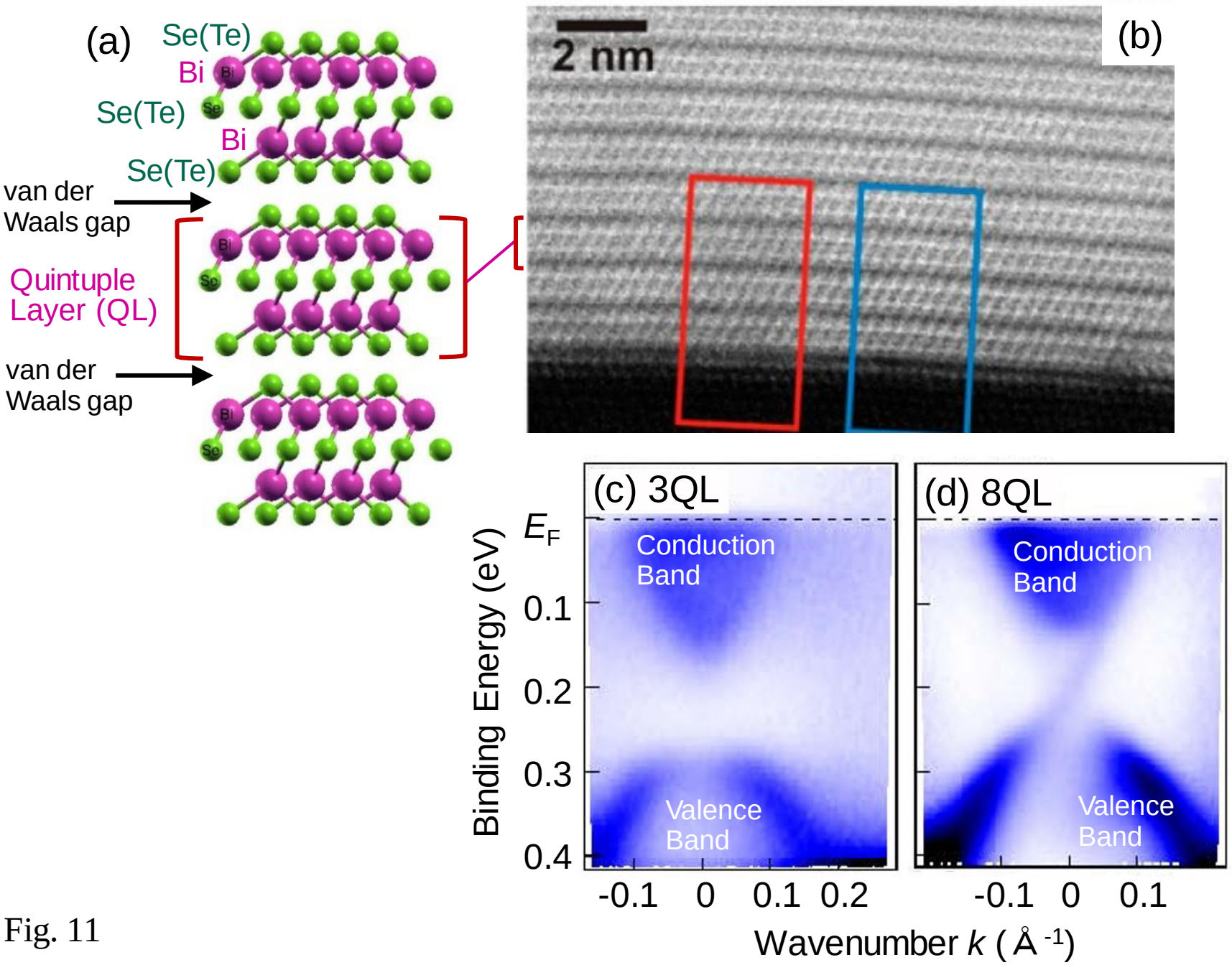
(a)
Se(Te)
Bi
Se(Te)
Bi
Se(Te)
van der
Waals gap
Quintuple
Layer (QL)
van der
Waals gap
2 nm
(b)
(c) 3QL
(d) 8QL
E_F
Conduction
Band
Valence
Band
Binding Energy (eV)
0.1
0.2
0.3
0.4
-0.1
0
0.1
0.2
Wavenumber k (Å $^{-1}$)

Fig. 11

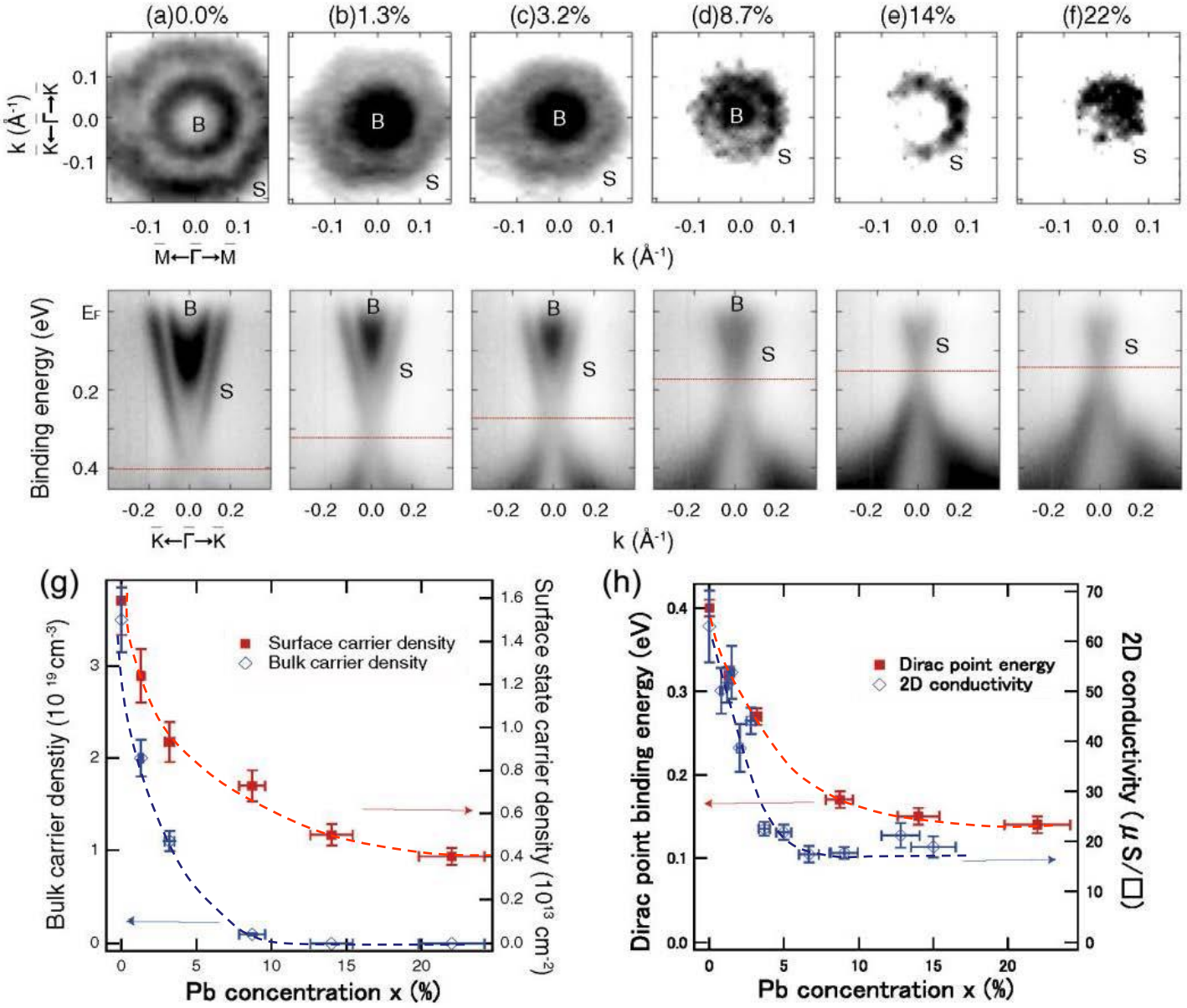
(a)0.0%
(b)1.3%
(c)3.2%
(d)8.7%
(e)14%
(f)22%
k (Å-1)
K̄←Γ̄→K̄
M̄←Γ̄→M̄
B
S
Binding energy (eV)
EF
(g)
Surface carrier density
Bulk carrier density
Bulk carrier denstiy (10 19 cm-3)
Surface state carrier density (1013 cm-2)
Pb concentration x (%)
(h)
Dirac point energy
2D conductivity
Dirac point binding energy (eV)
2D conductivity (μS/□)

Fig. 12

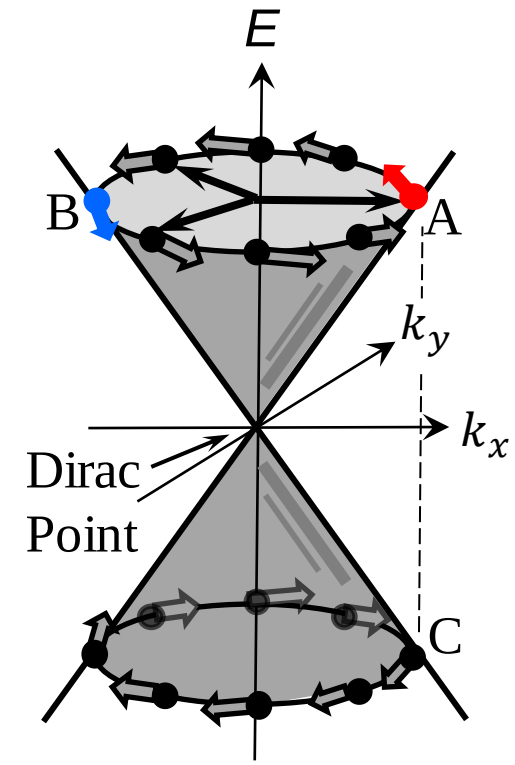

(a)

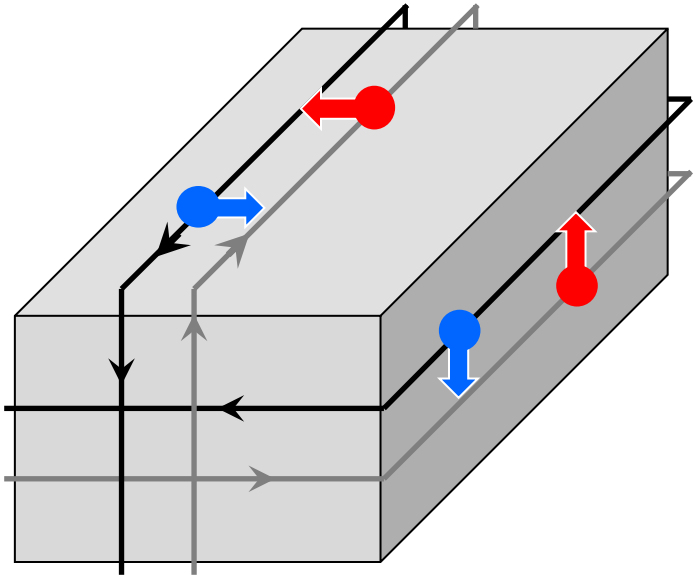

(c)

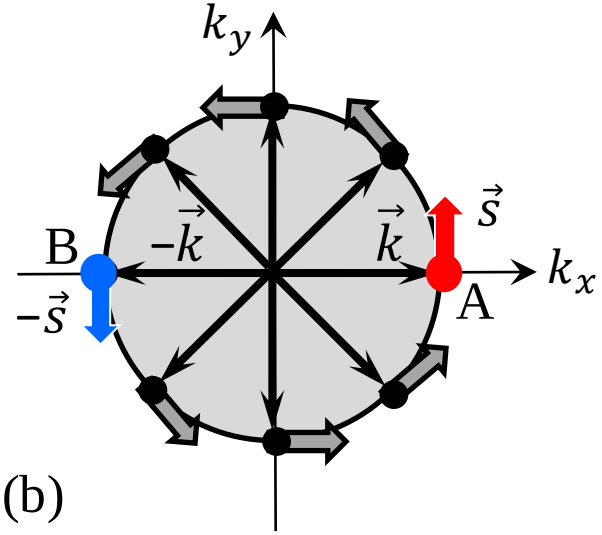

(b)

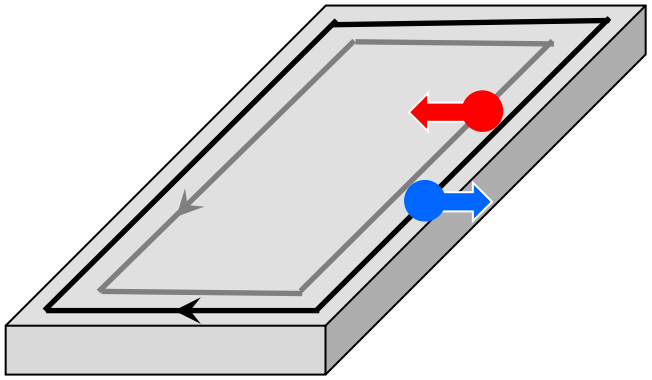

(d)

Fig. 13

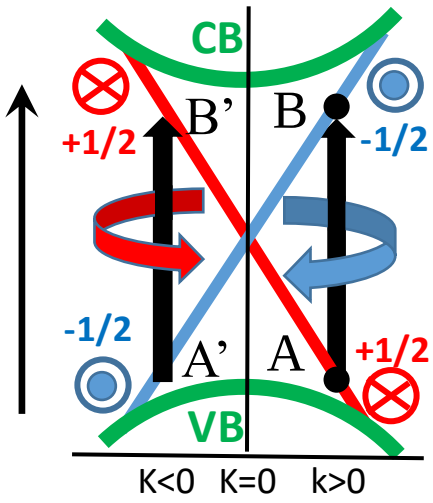
CB
B'
B
+1/2
-1/2
-1/2
A'
A
+1/2
VB
K<0
K=0
k>0

(a)

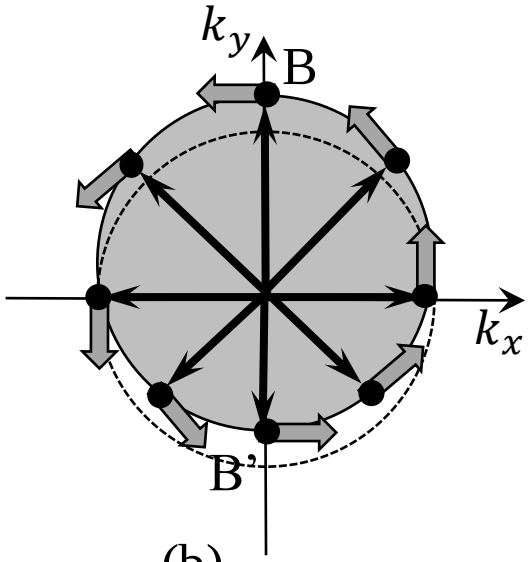
k_y
B
k_x
B'

(b)

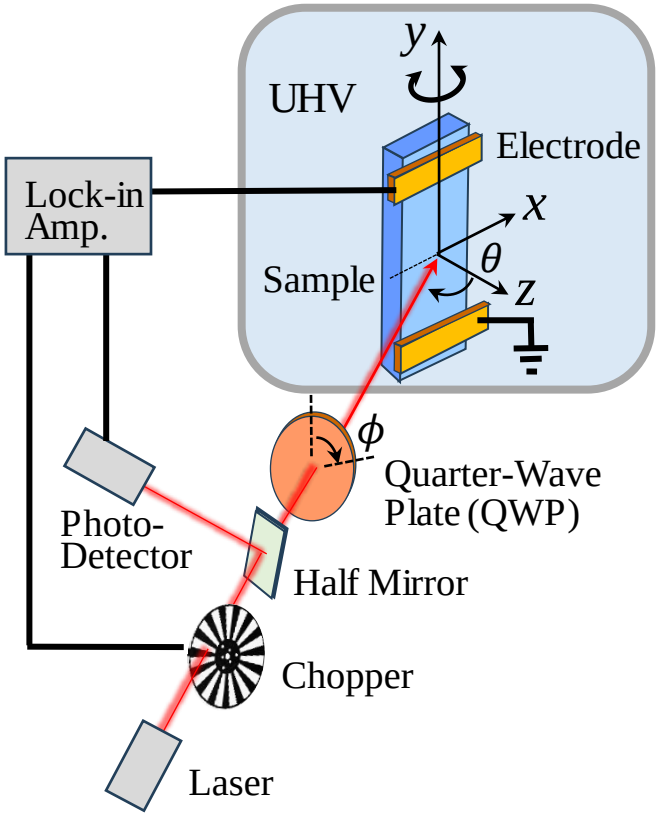
UHV
Electrode
Lock-in Amp.
Sample
y
x
θ
z
ϕ
Quarter-Wave Plate (QWP)
Photo-Detector
Half Mirror
Chopper
Laser

(c)

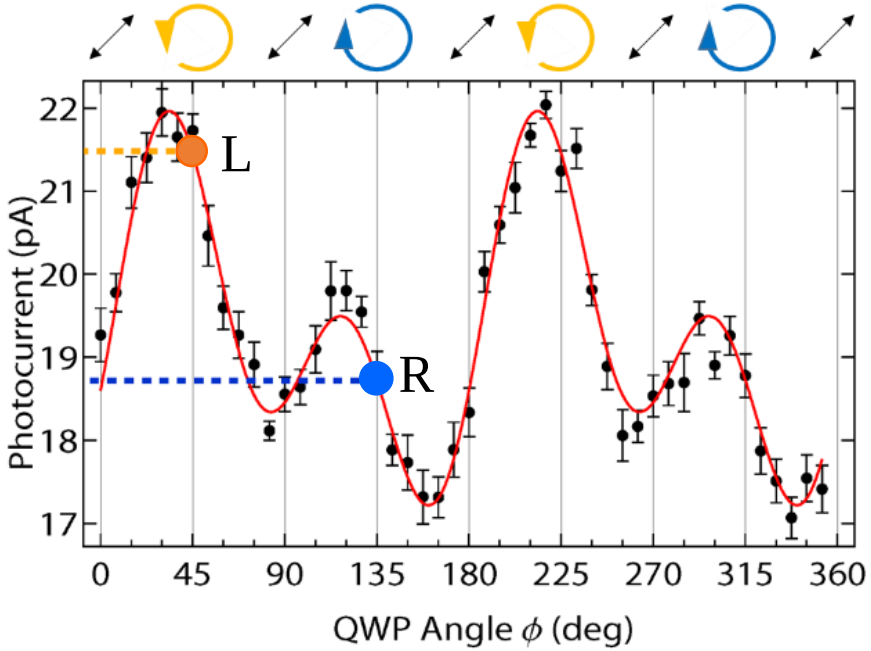
Photocurrent (pA)
22
21
20
19
18
17
L
R
0
45
90
135
180
225
270
315
360
QWP Angle ϕ (deg)

(d)

Fig. 14

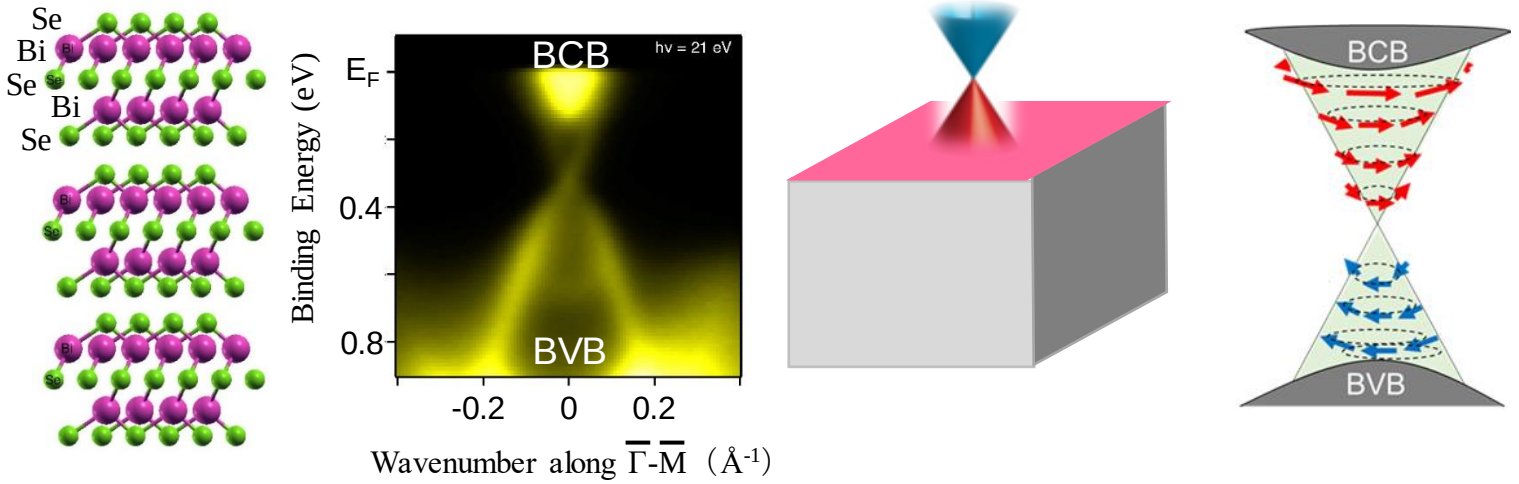

(a) Bi_2Se_3

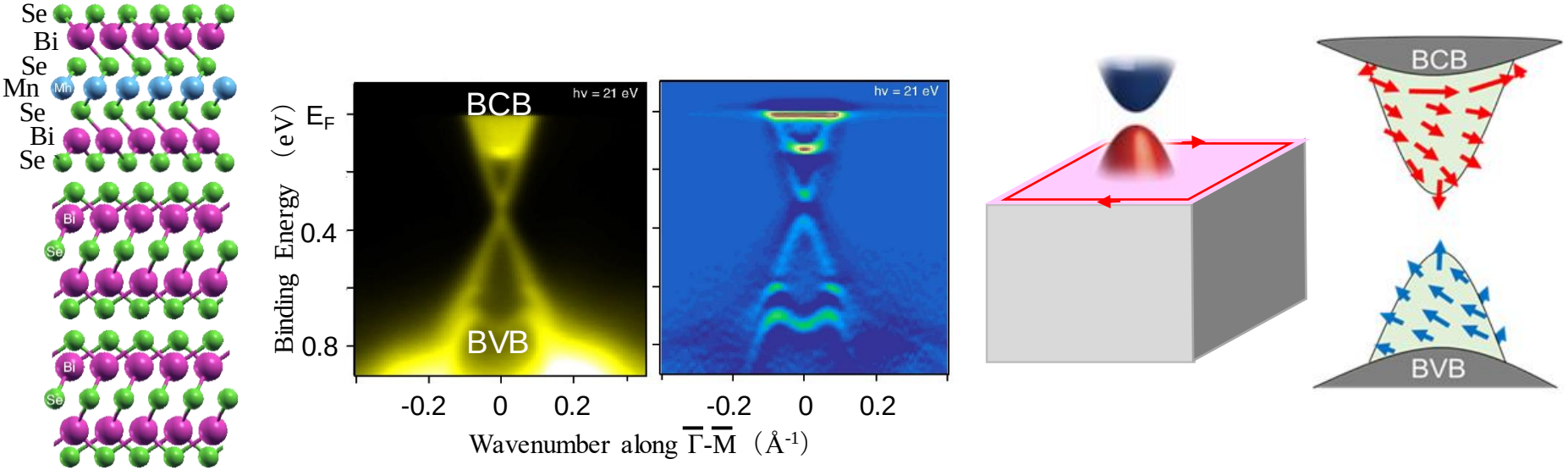

(b) $MnBi_2Se_4$ / Bi_2Se_3

Fig. 15

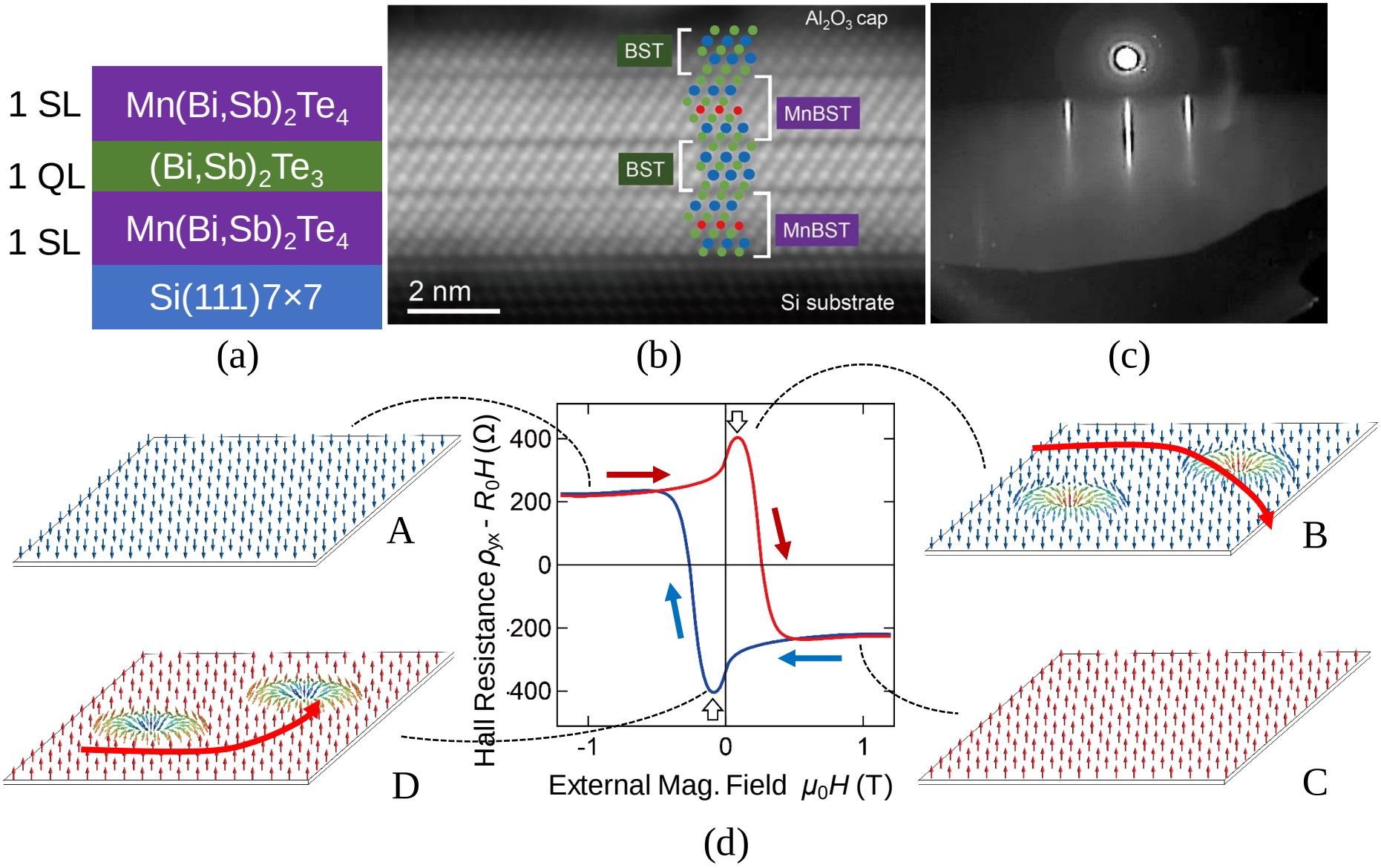
1 SL
Mn(Bi,Sb)2Te4
1 QL
(Bi,Sb)2Te3
1 SL
Mn(Bi,Sb)2Te4
Si(111)7×7
(a)
Al2O3 cap
BST
MnBST
BST
MnBST
2 nm
Si substrate
(b)
(c)
A
B
C
D
Hall Resistance ρyx - R0H (Ω)
400
200
0
-200
-400
-1
0
1
External Mag. Field μ0H (T)
(d)

Fig. 16